Phil. Trans. Roy. Soc. (Lond.) **B** (2001) **356**, 1-32

Geometric Visual Hallucinations, Euclidean Symmetry, and the Functional Architecture of Striate Cortex

Paul C. Bressloff[1]*, Jack D. Cowan[2]‡, Martin Golubitsky[3]
Peter J. Thomas[2]†and Matthew C. Wiener[4]

[1]*Department of Mathematical Sciences, Loughborough University*
Loughborough, Leicestershire LE11 3TU, U. K
[2]*Department of Mathematics, University of Chicago, Chicago Il 60637*
(cowan@math.uchicago.edu)
[3]*Department of Mathematics, University of Houston,*
Houston, TX 77204-3476
[4]*Laboratory of Neuropsychology, NIH, Bethesda, MD 20892*

*Current address: Department of Mathematics, University of Utah,Salt Lake City, Utah, 84112
†Current address: Computational Neurobiology Laboratory and Sloan Center for Theoretical Neurobiology, Salk Institute for Biological Studies, PO Box 85800, San Diego CA 92186-5800.

‡Correspondence should be sent to:
Professor Jack D. Cowan
Department of Mathematics, University of Chicago
5734 S. University Avenue, Chicago IL 60637
Tel: +1-(1)773-702-1076; Fax: +1-(1)773-702-9787
E-mail: cowan@math.uchicago.edu

[Key words: hallucinations, visual imagery, flicker phosphenes, neural modelling, horizontal connections, contours]

Contents

Summary

This paper is concerned with a striking visual experience: that of seeing geometric visual hallucinations. Hallucinatory images were classified by Klüver into four groups called form constants comprising (a) gratings, lattices, fretworks, filigrees, honeycombs and checkerboards (b) cobwebs (c) tunnels, funnels, alleys, cones and vessels and (d) spirals. This paper describes a mathematical investigation of their origin based on the assumption that the patterns of connection between retina and striate cortex (henceforth referred to as V1)—the retino-cortical map—and of neuronal circuits in V1, both local and lateral, determine their geometry.

In the first part of the paper we show that form constants, when viewed in V1 coordinates, correspond essentially to combinations of plane waves, the wavelengths of which are integral multiples of the width of a human Hubel–Wiesel hypercolumn, about $1.33 - 2.00$ mm. We next introduce a mathematical description of the large–scale dynamics of V1 in terms of the continuum limit of a lattice of interconnected hypercolumns, each of which itself comprises a number of interconnected iso–orientation columns. We then show that the patterns of interconnection in V1 exhibit a very interesting symmetry, i.e., they are invariant under the action of the planar Euclidean group $\mathbf{E}(2)$—the group of rigid motions in the plane—rotations, reflections and translations. What is novel is that the lateral connectivity of V1 is such that a new group action is needed to represent its properties: by virtue of its anisotropy it is invariant with respect to certain shifts and twists of the plane. It is this shift–twist invariance that generates new representations of $\mathbf{E}(2)$. Assuming that the strength of lateral connections is weak compared with that of local connections, we next calculate the eigenvalues and eigenfunctions of the cortical dynamics, using Rayleigh–Schrödinger perturbation theory. The result is that in the absence of lateral connections, the eigenfunctions are degenerate, comprising both even and odd combinations of sinusoids

in ϕ, the cortical label for orientation preference, and plane waves in $\mathbf{r}$, the cortical position coordinate. 'Switching–on' the lateral interactions breaks the degeneracy and either even or else odd eigenfunctions are selected. These results can be shown to follow directly from the Euclidean symmetry we have imposed.

In the second part of the paper we study the nature of various even and odd combinations of eigenfunctions or planforms, whose symmetries are such that they remain invariant under the particular action of $\mathbf{E}(2)$ we have imposed. These symmetries correspond to certain subgroups of $\mathbf{E}(2)$, the so–called axial subgroups. Axial subgroups are important in that the equivariant branching lemma indicates that when a symmetric dynamical system goes unstable, new solutions emerge which have symmetries corresponding to the axial subgroups of the underlying symmetry group. This is precisely the case studied in this paper. Thus we study the various planforms that emerge when our model V1 dynamics goes unstable under the presumed action of hallucinogens or flickering lights. We show that the planforms correspond to the axial subgroups of $\mathbf{E}(2)$, under the shift–twist action. We then compute what such planforms would look like in the visual field, given an extension of the retino–cortical map to include its action on local edges and contours. What is most interesting is that given our interpretation of the correspondence between V1 planforms and perceived patterns, the set of planforms generates representatives of all the form constants. It is also noteworthy that the planforms derived from our continuum model naturally divide V1 into what are called linear regions, in which the pattern has a near constant orientation, reminiscent of the iso–orientation patches constructed via optical imaging. The boundaries of such regions form fractures whose points of intersection correspond to the well–known 'pinwheels'.

To complete the study we then investigate the stability of the planforms, using methods of nonlinear stability analysis, including Liapunov–Schmidt reduction and Poincaré–Lindstedt perturbation theory. We find a close correspondence between stable planforms and form constants. The results are sensitive to the detailed specification of the lateral connectivity and suggest an interesting possibility, that the cortical mechanisms by which geometric visual hallucinations are generated, if sited mainly in V1, are closely related to those involved in the processing of edges and contours.

... the hallucination is ... not a static process
but a dynamic process, the instability of which
reflects an instability in its conditions of origin
Klüver (1966a) in a comment on Mourgue (1932)

1 Introduction

1.1 Form constants and visual imagery

Geometric visual hallucinations are seen in many situations, for example: after being exposed to flickering lights (Purkinje, 1918; Helmholtz, 1925; Smythies, 1960), after the administration of certain anaesthetics (Winters, 1975), on waking up or falling asleep (Dybowski, 1939), following deep binocular pressure on one's eyeballs (Tyler, 1978), and shortly after the ingesting of drugs such as LSD and Marihuana (Oster, 1970; Siegel, 1977). Patterns that may be hallucinatory are found preserved in petroglyphs (Patterson, 1992) and in cave paintings (Clottes & Lewis-Williams, 1998). There are many reports of such experiences (Knauer & Maloney, 1913):

> Immediately before my open eyes are a vast number of rings, apparently made of extremely fine steel wire, all constantly rotating in the direction of the hands of a clock; these circles are concentrically arranged, the innermost being infinitely small, almost pointlike, the outermost being about a meter and a half in diameter. The spaces between the wires seem brighter than the wires themselves. Now the wires shine like dim silver in parts. Now a beautiful light violet tint has developed in them. As I watch, the center seems to recede into the depth of the room, leaving the periphery stationary, till the whole assumes the form of a deep tunnel of wire rings. The light, which was irregularly distributed among the circles, has receded with the center into the apex of the funnel. The center is gradually returning, and passing the position when all the rings are in the same vertical plane, continues to advance, till a cone forms with its apex toward me ... The wires are now flattening into bands or ribbons, with a suggestion of transverse striation, and colored a gorgeous ultramarine blue, which passes in places into an intense sea green. These bands move rhythmically, in a

> wavy upward direction, suggesting a slow endless procession of small mosaics, ascending the wall in single files. The whole picture has suddenly receded, the center much more than the sides, and now in a moment, high above me, is a dome of the most beautiful mosiacs, ... The dome has absolutely no discernible pattern. But circles are now developing upon it; the circles are becoming sharp and elongated ... now they are rhombics now oblongs; and now all sorts of curious angles are forming; and mathematical figures are chasing each other wildly across the roof ...

Klüver (1966b) organized the many reported images into four classes, which he called form constants:(I) gratings, lattices, fretworks, filigrees, honeycombs and checkerboards (II) cobwebs (III) tunnels and funnels, alleys, cones, vessels, and (IV) spirals. Some examples of class I form constants are shown in figure 1, while examples of the

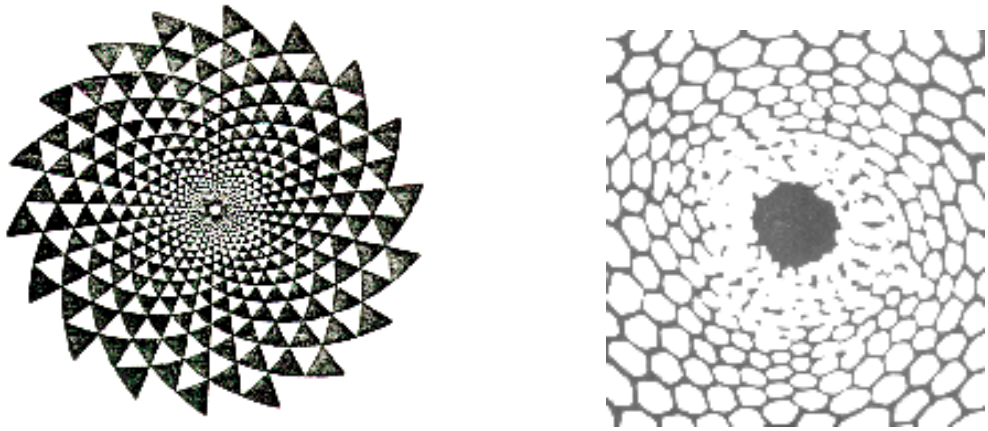

Figure 1: Left panel: 'Phosphene' produced by deep binocular pressure on the eyeballs. Redrawn from Tyler (1978). Right panel: Honeycomb hallucination generated by Marihuana. Redrawn from Clottes & Lewis-Williams (1998).

other classes are shown in figures 2–4.

Such images are seen both by blind subjects and in sealed dark rooms (Krill, Alpert, & Ostfield, 1963). Various reports (Klüver, 1966b) indicate that although they are difficult to localize in space, they are stable with respect to eye movements,

Figure 2: Funnel and Spiral hallucinations generated by LSD. Redrawn from Oster (1970)

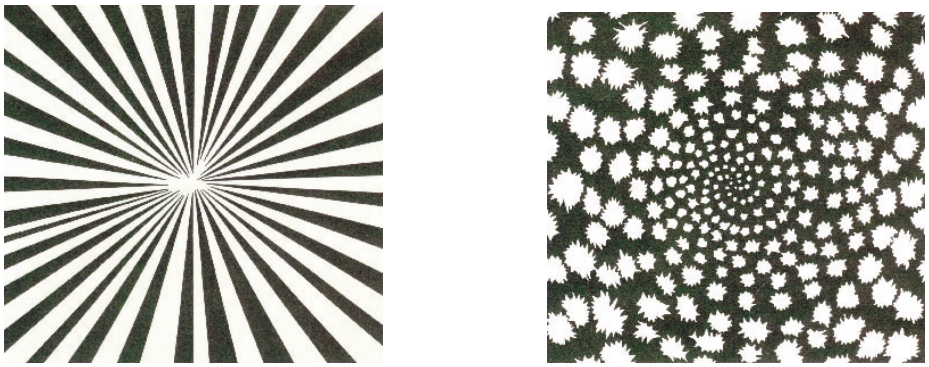

Figure 3: Funnel and Spiral Tunnel Hallucinations generated by LSD. Redrawn from Siegel (1977).

Figure 4: Cobweb petroglyph. Redrawn from Patterson (1992).

i.e., they remain fixed in the visual field. This suggests that they are generated not in the eyes, but somewhere in the brain. One clue on their location in the brain is provided by recent studies of visual imagery (Miyashita, 1995). Although controversial, the evidence seems to suggest that areas V1 and V2, the striate and extra–striate visual cortices, are involved in visual imagery, particularly if the image requires detailed inspection (Kosslyn, 1994). More precisely, it has been suggested that (Ishai & Sagi, 1995):

> [the] topological representation [provided by V1] might subserve visual imagery when the subject is scrutinizing attentively local features of objects that are stored in memory.

Thus visual imagery is seen as the result of an interaction between mechanisms subserving the retrieval of visual memories and those involving focal attention. In this respect it is interesting that there seems to be competition between the seeing of visual imagery and hallucinations (Knauer & Maloney, 1913) :

> ...after a picture had been placed on a background and then removed "I tried to see the picture with open eyes. In no case was I successful; only [hallucinatory] visionary phenomena covered the ground".

Competition between hallucinatory images and after–images has also been reported (Klüver, 1966b):

> In some instances, the [hallucinatory] visions prevented the appearance of after–images entirely; [however] in most cases a sharply outlined normal after–image appeared for a while....while the visionary phenomena were stationary, the after–images moved with the eyes

As pointed out to us by one of the referees, the fused image of a pair of random dot stereograms also seems to be stationary with respect to eye movements. It has also be argued that since hallucinatory images are seen as continuous across the mid–line, they must be located at higher levels in the visual pathway than V1 or V2 [R. Shapley, personal communication.] In this respect there is evidence that callosal connections along the V1/V2 border can act to maintain continuity of the images across the vertical meridian (Hubel & Wiesel, 1967).

All these observations suggest that both areas V1 and V2 are involved in the generation of hallucinatory images. In our view such images are generated in V1 and stabilized with respect to eye movements by mechanisms present in V2 and elsewhere. It is likely that the action of such mechanisms is rapidly fed–back to V1 (Lee, Mumford, Romero, & Lamme, 1998). It now follows, since all observers report seeing Klüver's form constants or variations, that those properties common to all such hallucinations should yield information about the architecture of V1. We therefore investigate that architecture, i.e., the patterns of connection between neurons in the retina and those in V1, together with intracortical V1 connections, on the hypothesis that such patterns determine, in large part, the geometry of hallucinatory form constants, and we defer until a later study, the investigation of mechanisms that contribute to their continuity across the midline and to their stability in the visual field.

1.2 The human retino–cortical map

The first step is to calculate what visual hallucinations look like, not in the standard polar coordinates of the visual field, but in the coordinates of V1. It is well established

that there is a topographic map of the visual field in V1, the retinotopic representation, and that the central region of the visual field has a much bigger representation in V1 than it does in the visual field (Sereno, Dale, Reppas, Kwong, Belliveau, Brady, Rosen, & Tootell, 1995). The reason for this is partly that there is a non–uniform distribution of retinal ganglion cells, each of which connects to V1 via the lateral geniculate nucleus (LGN). This allows calculation of the details of the map (Cowan, 1977). Let ρ_R be the packing density of retinal ganglion cells, per unit area of the visual field, ρ the corresponding density per unit surface area of cells in V1, and $[r_R, \theta_R]$ retinal or equivalently, visual field coordinates. Then $\rho_R r_R dr_R d\theta_R$ is the number of ganglion cell axons in a retinal element of area $r_R dr_R d\theta_R$. By hypothesis these axons connect topographically to cells in an element of V1 surface area $dxdy$, i.e. to $\rho dxdy$ cortical cells. [V1 is assumed to be locally flat with Cartesian coordinates]. Empirical evidence indicates that ρ is approximately constant (Hubel & Wiesel, 1974a,b), whereas ρ_R declines from the origin of the visual field, i.e. the *fovea*, with an inverse square law (Drasdo, 1977):

$$\rho_R = \frac{1}{(w_0 + \epsilon r_R)^2}.$$

where w_0 and ϵ are constants. Estimates of $w_0 = 0.087$ and $\epsilon = 0.051$ in appropriate units can be obtained from published data (Drasdo, 1977). From this one can calculate the Jacobian of the map and hence V1 coordinates $\{x, y\}$ as functions of visual field or retinal coordinates $\{r_R, \theta_R\}$. The resulting coordinate transformation takes the form:

$$x = \frac{\alpha}{\epsilon} \ln \left[1 + \frac{\epsilon}{w_0} r_R \right], \; y = \frac{\beta r_R \theta_R}{w_0 + \epsilon r_R},$$

where α and β are constants in appropriate units. Figure 5 shows the map.

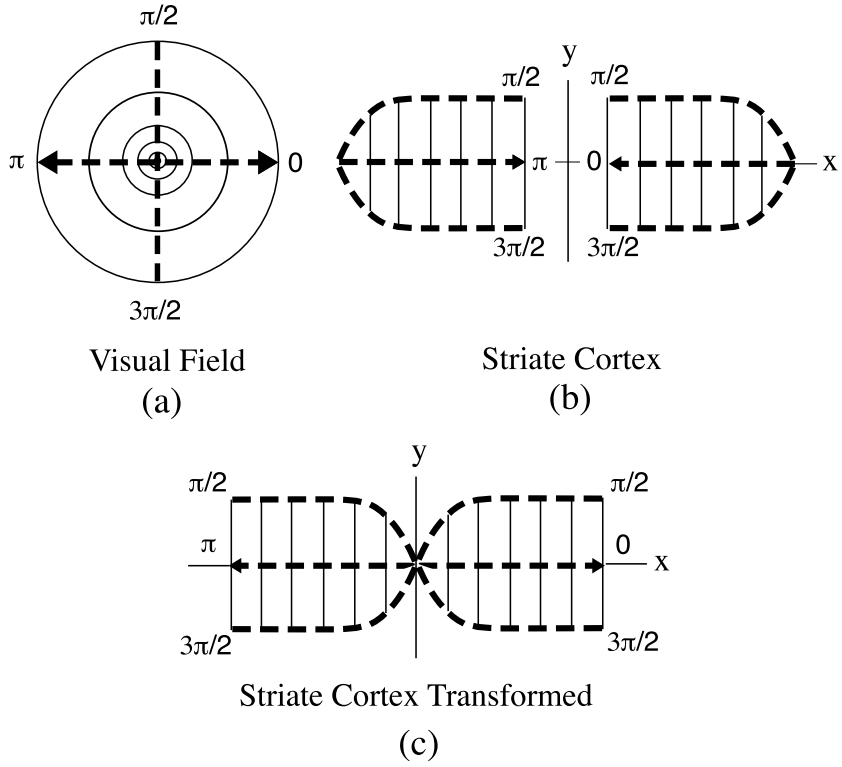

Figure 5: The retino–cortical map. (a) Visual field, (b) The actual cortical map, comprising right and left hemisphere transforms, (c) A transformed version of the cortical map. The two transforms are realigned so that both foveal regions correspond to $x = 0$.

The transformation has two important limiting cases: (a) near the fovea, $\epsilon r_R < w_0$, it reduces to:

$$x = \frac{\alpha r_R}{w_0},\ y = \frac{\beta r_R\, \theta_R}{w_0}.$$

and (b), sufficiently far away from the fovea, $\epsilon r_R \gg w_0$, it becomes:

$$x = \frac{\alpha}{\epsilon}\ \ln \frac{\epsilon\, r_R}{w_0},\ y = \frac{\beta \theta_R}{\epsilon}.$$

(a) is just a scaled version of the identity map, and (b) is a scaled version of the complex logarithm as was first recognized by Schwartz (1977). To see this let $z_R =$

$x_R + iy_R = r_R \exp[i\theta_R]$, be the complex representation of a retinal point $(x_R, y_R) = (r_R, \theta_R)$, then $z = x + iy = \ln(r_R \exp[i\theta_R]) = \ln r_R + i\theta_R$. Thus $x = \ln r_R, y = \theta_R$.

1.3 Form constants as spontaneous cortical patterns

Given that the retino–cortical map is generated by the complex logarithm (except near the fovea), it is easy to calculate the action of the transformation on circles, rays, and logarithmic spirals in the visual field. Circles of constant r_R in the visual field become vertical lines in V1, whereas rays of constant θ_R become horizontal lines. Interestingly, logarithmic spirals become oblique lines in V1: the equation of such a spiral is just $\theta_R = a \ln r_R$ whence $y = ax$ under the action of $z_R \to z$. Thus form constants comprising circles, rays, and logarithmic spirals in the visual field correspond to stripes of neural activity at various angles in V1. Figures 6 and 7 show the map action on the funnel and spiral form constants shown in figure 2.

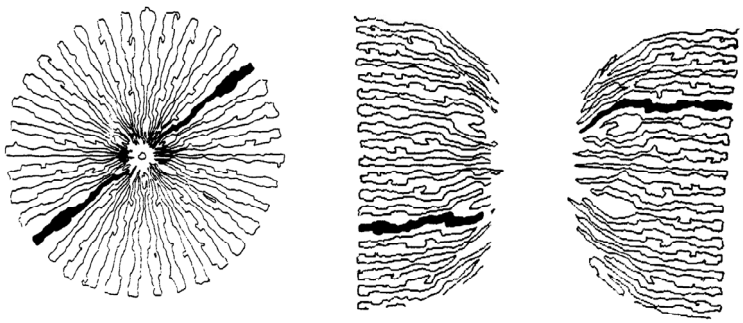

Figure 6: Action of the retino–cortical map on the funnel form constant. (a) Image in the visual field, (b) V1 map of the image.

A possible mechanism for the spontaneous formation of stripes of neural activity under the action of hallucinogens was originally proposed by Ermentrout & Cowan (1979). They studied interacting populations of excitatory and inhibitory neurons distributed within a two–dimensional cortical sheet. Modeling the evolution of the system in terms of a set of Wilson–Cowan equations (Wilson & Cowan, 1972, 1973)

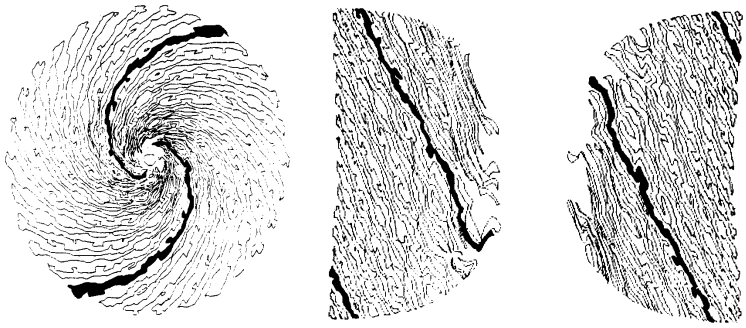

Figure 7: Action of the retino–cortical map on the spiral form constant. (a) Image in the visual field, (b) V1 map of the image.

they showed how spatially periodic activity patterns such as stripes can bifurcate from a homogeneous low–activity state via a Turing–like instability (Turing, 1952). The model also supports the formation of other periodic patterns such as hexagons and squares—under the retino–cortical map these generate more complex hallucinations in the visual field such as checkerboards. Similar results are found in a reduced single–population model provided that the interactions are characterized by a mixture of short–range excitation and long–range inhibition (the so–called 'Mexican hat distribution').

1.4 Orientation tuning in V1

The Ermentrout–Cowan theory of visual hallucinations is over–simplified in the sense that V1 is represented as if it were just a cortical retina. However V1 cells do much more than merely signalling position in the visual field: most cortical cells signal the local orientation of a contrast edge or bar—they are tuned to a particular local orientation (Hubel & Wiesel, 1974a). The absence of orientation representation in the Ermentrout–Cowan model means that a number of the form constants cannot be generated by the model including lattice tunnels (figure 42), honeycombs and certain checkerboards (figure 1), and cobwebs (figure 4). These hallucinations, except

the checkerboards, are more accurately characterized as lattices of locally oriented contours or edges rather than in terms of contrasting regions of light and dark.

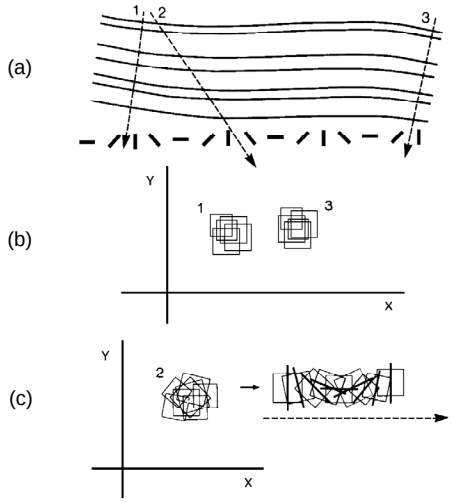

Figure 8: (a) Orientation tuned cells in V1. Note the constancy of orientation preference at each cortical location [electrode tracks 1 and 3], and the rotation of orientation preference as cortical location changes [electrode track 2], (b) receptive fields for tracks 1 and 3, (c) expansion of the recptive fields of track 2 to show rotation of orientation preferences. Redrawn from Gilbert (1992).

In recent years much information has accumulated about the distribution of orientation selective cells in V1, and about their pattern of interconnection (Gilbert, 1992). Figure 8 shows a typical arrangement of such cells, obtained via microelectrodes implanted in Cat V1. The first panel shows how orientation preferences rotate smoothly over V1, so that approximately every 300 μm the same preference reappears, i.e. the distribution is π–periodic in the orientation preference angle. The second panel shows the receptive fields of the cells, and how they change with V1 location. The third panel shows more clearly the rotation of such fields with translation across V1.

How are orientation tuned cells distributed and interconnected? Recent work on optical imaging has made it possible to see how the cells are actually distributed in V1 (Blasdel, 1992), and a variety of stains and labels have made it possible to see

how they are interconnected (Blasdel and Sincich, personal communication), (Eysel, 1999; Bosking, Zhang, Schofield, & Fitzpatrick, 1997). Figures 9–10 show such data.

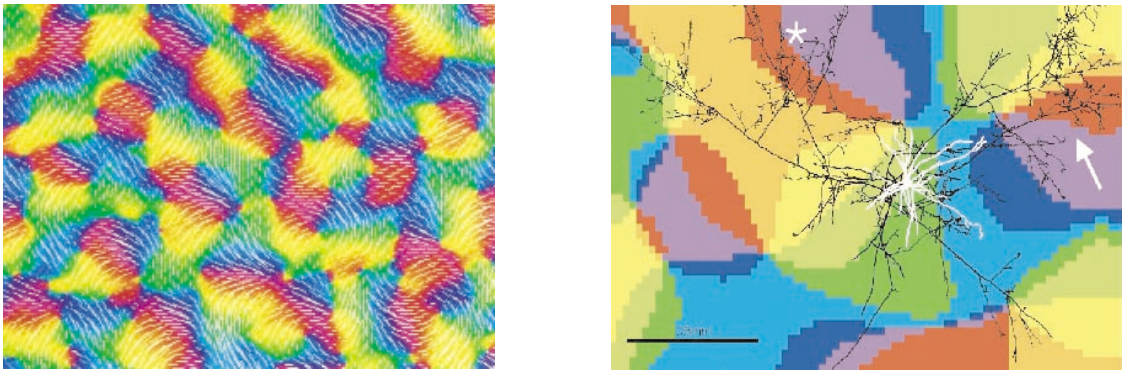

Figure 9: Left panel: Distribution of orientation preferences in Macaque V1 obtained via optical imaging. Redrawn from Blasdel (1992); Right panel: Connections made by an inhibitory interneuron in Cat V1. Redrawn from Eysel (1999).

Thus, the left panel of Figure 9 shows that the distribution of orientation preferences is indeed roughly π–periodic, in that approximately every 0.5 mm (in the Macaque) there is an iso–orientation patch of a given preference, and Figure 10 that there seem to be at least two length–scales:

(a) local – cells less than 0.5 mm apart tend to make connections with most of their neighbors in a roughly isotropic fashion, as seen in the right panel of Figure 9, and

(b) lateral – cells make contacts only every 0.5 mm or so along their axons with cells in similar iso–orientation patches.

In addition, Figure 10 shows that the long axons which support such connections, known as intrinsic lateral or horizontal connections, and found mainly in layers II and III of V1, and to some extent in layer V (Rockland & Lund, 1983), tend to be oriented along the direction of their cells preference (Gilbert, 1992; Bosking *et al.*, 1997), i.e., they run parallel to the visuotopic axis of their cell's orientation preference.

These horizontal connections arise almost exclusively from excitatory neurons (Levitt & Lund, 1997; Gilbert & Wiesel, 1983), although 20% terminate on inhibitory cells and can thus have significant inhibitory effects (McGuire, Gilbert, Rivlin, & Wiesel, 1991).

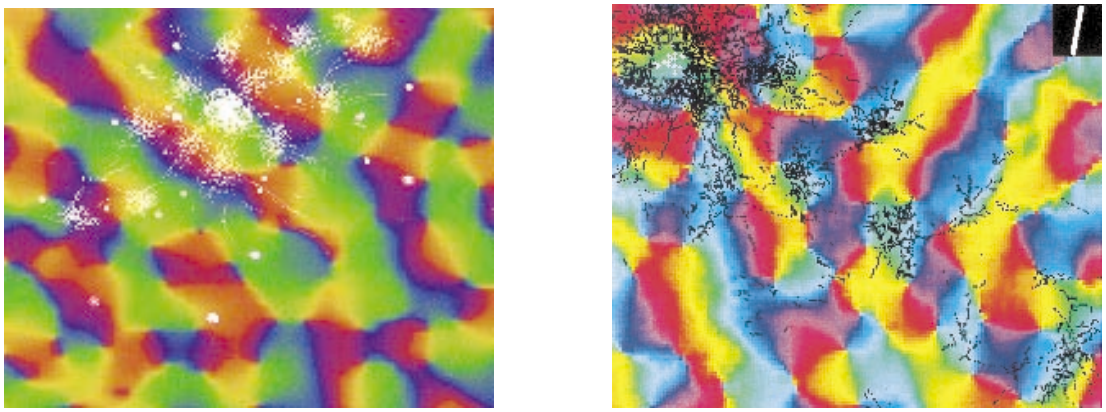

Figure 10: Lateral Connections made by V1 cells in Owl Monkey (Left panel) and Tree Shrew (Right panel) V1. A radioactive tracer is used to show the locations of all terminating axons from cells in a central injection site, superimposed on an orientation map obtained by optical imaging. Redrawn from Blasdel & Sincich [personal communication] and Bosking *et al.* (1997).

There is some anatomical and psychophysical evidence (Horton, 1996; Tyler, 1982) that Human V1 has several times the surface area of Macaque V1 with a hypercolumn spacing of about $1.33 - 2$ mm. In the rest of this paper we work with this length–scale to extend the Ermentrout–Cowan theory of visual hallucinations to include orientation selective cells. A preliminary account of this was described in Wiener (1994) and Cowan (1997).

2 A model of V1 with anisotropic lateral connections

2.1 The model

The state of a population of cells comprising an iso–orientation patch at cortical position $\mathbf{r} \in \mathbf{R}^2$ at time t is characterized by the real–valued activity variable $a(\mathbf{r}, \phi, t)$, where $\phi \in [0, \pi)$ is the orientation preference of the patch. V1 is treated as an (unbounded) continuous two-dimensional sheet of nervous tissue. For the sake of analytical tractability, we make the additional simplifying assumption that ϕ and $\mathbf{r}$ are independent variables – all possible orientations are represented at every position. A more accurate model would need to incorporate details concerning the distribution of orientation patches in the cortical plane (as illustrated in figure 9). It is known, for example, that a region of human V1 roughly 2.67 mm^2 on its surface and extending throughout its depth contains at least two sets of all iso-orientation patches in the range $0 \leq \phi < \pi$, one for each eye. Such a slab was called a hypercolumn by (Hubel & Wiesel, 1974b). If human $V1$ as a whole (in one hemisphere) has a surface area of about 3500 mm^2(Horton, 1996), this gives approximately 1300 such hypercolumns. So one interpretation of our model would be that it is a continuum version of a lattice of hypercolumns. However, a potential difficulty with this interpretation is that the effective wavelength of many of the patterns underlying visual hallucinations is of the order of twice the hypercolumn spacing (see for example figure 2), suggesting that lattice effects might be important. A counter argument for the validity of the continuum model (besides mathematical convenience) is to note that the separation of two points in the visual field—visual acuity—(at a given retinal eccentricity of $\mathbf{r}_R^o$), corresponds to hypercolumn spacing (Hubel & Wiesel, 1974b), and so to each location in the visual field there corresponds a representation in V1 of that location with finite resolution and all possible orientations.

The activity variable $a(\mathbf{r}, \phi, t)$ evolves according to a generalization of the Wilson–Cowan equations (Wilson & Cowan, 1972, 1973) that takes into account the additional

internal degree of freedom arising from orientation preference:

$$\frac{\partial a(\mathbf{r},\phi,t)}{\partial t} = -\alpha a(\mathbf{r},\phi,t) + \mu \int_0^\pi \int_{\mathbf{R}^2} w(\mathbf{r},\phi|\mathbf{r}',\phi')\sigma[a(\mathbf{r}',\phi',t)]\frac{d\mathbf{r}'d\phi'}{\pi} + h(\mathbf{r},\phi,t) \quad (2.1)$$

where α and μ are decay and coupling coefficients, $h(\mathbf{r},\phi,t)$ is an external input, $w(\mathbf{r},\phi|\mathbf{r}',\phi')$ is the weight of connections between neurons at $\mathbf{r}$ tuned to ϕ and neurons at $\mathbf{r}'$ tuned to ϕ', and $\sigma[z]$ is the smooth nonlinear function

$$\sigma[z] = \frac{1}{1+\mathrm{e}^{-\gamma(z-\zeta)}} \quad (2.2)$$

for constants γ and ζ. Without loss of generality we may subtract from $\sigma[z]$ a constant equal to $[1+\mathrm{e}^{\gamma\zeta}]^{-1}$ to obtain the (mathematically) important property that $\sigma[0]=0$, which implies that for zero external inputs the homogeneous state $a(\mathbf{r},\phi,t)=0$ for all $\mathbf{r},\phi,t$ is a solution to equation (2.1). From the discussion in section §1.4, we take

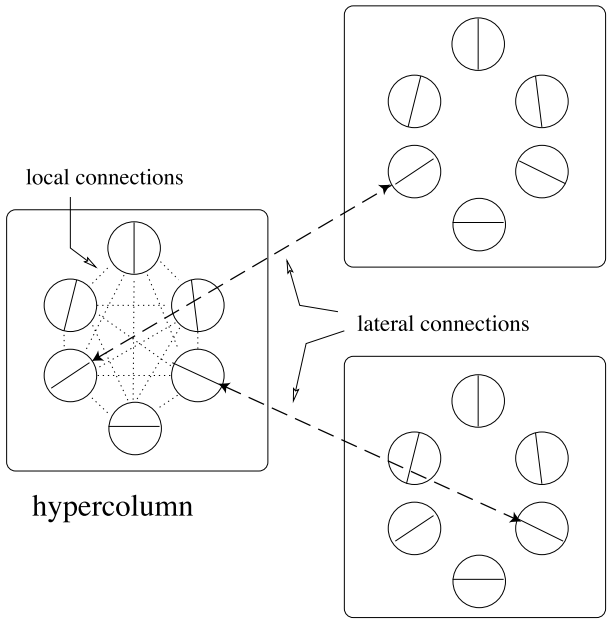

Figure 11: Illustration of the local connections within a hypercolumn and the anisotropic lateral connections between hypercolumns

the pattern of connections $w(\mathbf{r},\phi|\mathbf{r}',\phi')$ to satisfy the following properties (see figure 11):

(a) There exists a mixture of local connections within a hypercolumn and (anisotropic) lateral connections between hypercolumns; the latter only connect elements with the same orientation preference. Thus in the continuum model w is decomposed as

$$w(\mathbf{r},\phi|\mathbf{r}',\phi') = w_{loc}(\phi-\phi')\delta(\mathbf{r}-\mathbf{r}') + w_{lat}(\mathbf{r}-\mathbf{r}',\phi)\delta(\phi-\phi') \tag{2.3}$$

with $w_{loc}(-\phi) = w_{loc}(\phi)$.

(b) Lateral connections between hypercolumns only join neurons that lie along the direction of their (common) orientation preference ϕ. Thus in the continuum model

$$w_{lat}(\mathbf{r},\phi) = \hat{w}(R_{-\phi}\mathbf{r}) \tag{2.4}$$

with

$$\hat{w}(\mathbf{r}) = \int_0^\infty g(s)\left[\delta(\mathbf{r}-s\mathbf{r}_0)+\delta(\mathbf{r}+s\mathbf{r}_0)\right]ds \tag{2.5}$$

where $\mathbf{r}_0 = (1,0)$ and R_θ is the rotation matrix

$$R_\theta \begin{pmatrix} x \\ y \end{pmatrix} = \begin{pmatrix} \cos\theta & -\sin\theta \\ \sin\theta & \cos\theta \end{pmatrix}\begin{pmatrix} x \\ y \end{pmatrix}.$$

The weighting function $g(s)$ determines how the strength of lateral connections varies with the distance of separation. We take $g(s)$ to be of the particular form

$$g(s) = [2\pi\xi_{lat}^2]^{-1/2}\mathrm{e}^{-s^2/2\xi_{lat}^2} - A_{lat}[2\pi\hat{\xi}_{lat}^2]^{-1/2}\mathrm{e}^{-s^2/2\hat{\xi}_{lat}^2} \tag{2.6}$$

with $\xi_{lat} < \hat{\xi}_{lat}$ and $A_{lat} \leq 1$, which represents a combination of short-range excitation and long-range inhibition. This is an example of the Mexican hat distribution. (Note that one can view the short–range excitatory connections as arising from patchy local connections within a hypercolumn).

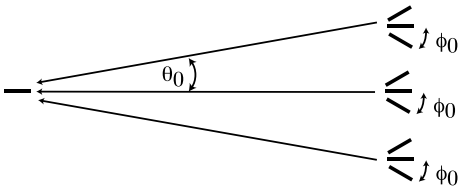

Figure 12: Example of an angular spread in the anisotropic lateral connections between hypercolumns with respect to both space (θ_0) and orientation preference (ϕ_0)

It is possible to consider more general choices of weight distribution w that (i) allow for some spread in the distribution of lateral connections (see figure 12) and (ii) incorporate spatially extended isotropic local interactions. An example of such a distribution is given by the following generalization of equations (2.3) and (2.4):

$$w(\mathbf{r},\phi|\mathbf{r}',\phi') = w_{loc}(\phi-\phi')\Delta_{loc}(|\mathbf{r}-\mathbf{r}'|) + \hat{w}(R_{-\phi}[\mathbf{r}'-\mathbf{r}])\Delta_{lat}(\phi-\phi') \tag{2.7}$$

with $\Delta_{lat}(-\phi) = \Delta_{lat}(\phi)$, $\Delta_{lat}(\phi) = 0$ for $|\phi| > \phi_0$, and $\Delta_{loc}(|\mathbf{r}|) = 0$ for $\mathbf{r} > \xi_0$. Moreover, equation (2.5) is modified according to

$$\hat{w}(\mathbf{r}) = \int_{-\theta_0}^{\theta_0} p(\theta) \int_0^{\infty} g(s)\left[\delta(\mathbf{r}-s\mathbf{r}_\theta)+\delta(\mathbf{r}+s\mathbf{r}_\theta)\right] ds d\theta \tag{2.8}$$

with $\mathbf{r}_\theta = (\cos(\theta),\sin(\theta))$ and $p(-\theta) = p(\theta)$. The parameters ϕ_0 and θ_0 determine the angular spread of lateral connections with respect to orientation preference and space respectively, whereas ξ_0 determines the (spatial) range of the isotropic local connections.

2.2 Euclidean symmetry

Suppose that the weight distribution w satisfies equations (2.7) and (2.8). We show that w is invariant under the action of the Euclidean group $\mathbf{E}(2)$ of rigid motions in the plane, and discuss some of the important consequences of such a symmetry.

Euclidean group action The Euclidean group is composed of the (semi-direct) product of $\mathbf{O}(2)$, the group of planar rotations and reflections, with $\mathbf{R}^2$, the group of

planar translations. The action of the Euclidean group on $\mathbf{R}^2 \times \mathbf{S}^1$ is generated by:

$$\begin{aligned} \mathbf{s} \cdot (\mathbf{r}, \phi) &= (\mathbf{r} + \mathbf{s}, \phi) \quad \mathbf{s} \in \mathbf{R}^2 \\ \theta \cdot (\mathbf{r}, \phi) &= (R_\theta \mathbf{r}, \phi + \theta) \quad \theta \in \mathbf{S}^1 \\ \kappa \cdot (\mathbf{r}, \phi) &= (\kappa \mathbf{r}, -\phi), \end{aligned} \tag{2.9}$$

where κ is the reflection $(x_1, x_2) \mapsto (x_1, -x_2)$ and R_θ is a rotation by θ.

The corresponding group action on a function $a : \mathbf{R}^2 \times \mathbf{S}^1 \to \mathbf{R}$ where $P = (\mathbf{r}, \phi)$ is given by

$$\gamma \cdot a(P) = a(\gamma^{-1} \cdot P) \quad \text{for all } \gamma \in \mathbf{O}(2) \dot{+} \mathbf{R}^2 \tag{2.10}$$

and the action on $w(P|P')$ is

$$\gamma \cdot w(P|P') = w(\gamma^{-1} \cdot P | \gamma^{-1} \cdot P').$$

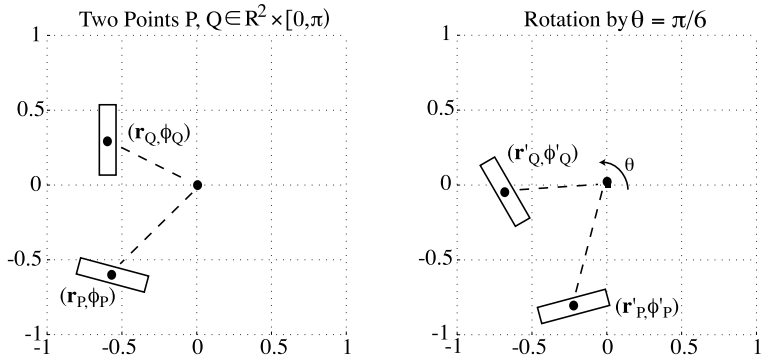

Figure 13: Action of a rotation by θ: $(\mathbf{r}, \phi) \to (\mathbf{r}', \phi') = (R_\theta \mathbf{r}, \phi + \theta)$

The particular form of the action of rotations in (2.9) reflects a crucial feature of the lateral connections, namely that they tend to be oriented along the direction of their cell's preference (see figure 11). Thus, if we just rotate V1, then the cells that are now connected at long range will not be connected in the direction of their preference. This difficulty can be overcome by permuting the local cells in each hypercolumn so that cells that are connected at long range are again connected in the direction of

their preference. Thus, in the continuum model, the action of rotation of V1 by θ corresponds to rotation of $\mathbf{r}$ by θ while simultaneously sending ϕ to $\phi + \theta$. This is illustrated in figure 13. The action of reflections is justified in a similar fashion.

Invariant weight distribution w**.** We now prove that w as given by equations (2.7) and (2.8) is invariant under the action of the Euclidean group defined by (2.9). (It then follows that the distribution satisfying equations (2.3)–(2.5) is also Euclidean invariant). Translation invariance of w is obvious, that is,

$$w(\mathbf{r}-\mathbf{s},\phi|\mathbf{r}'-\mathbf{s},\phi') = w(\mathbf{r},\phi|\mathbf{r}',\phi').$$

Invariance with respect to a rotation by θ follows from

$$\begin{aligned} &w(R_{-\theta}\mathbf{r},\phi-\theta|R_{-\theta}\mathbf{r}',\phi'-\theta) \\ &\quad = w_{loc}(\phi-\phi')\Delta_{loc}(|R_{-\theta}[\mathbf{r}-\mathbf{r}']|) + \hat{w}(R_{-\phi+\theta}R_{-\theta}(\mathbf{r}-\mathbf{r}'))\Delta_{lat}(\phi-\phi') \\ &\quad = w_{loc}(\phi-\phi')\Delta_{loc}(|\mathbf{r}-\mathbf{r}'|) + \hat{w}(R_{-\phi}\mathbf{r})\Delta_{lat}(\phi-\phi') \\ &\quad = w(\mathbf{r},\phi|\mathbf{r}',\phi') \end{aligned}$$

Finally, invariance under a reflection κ about the x-axis holds since

$$\begin{aligned} w(\kappa\mathbf{r},-\phi|\kappa\mathbf{r}',-\phi') &= w_{loc}(-\phi+\phi')\Delta_{loc}(|\kappa[\mathbf{r}-\mathbf{r}']|) + \hat{w}(R_{\phi}\kappa(\mathbf{r}-\mathbf{r}'))\Delta_{lat}(-\phi+\phi') \\ &= w_{loc}(\phi-\phi')\Delta_{loc}(|\mathbf{r}-\mathbf{r}'|) + \hat{w}(\kappa R_{\phi}(\mathbf{r}-\mathbf{r}'))\Delta_{lat}(\phi-\phi') \\ &= w_{loc}(\phi-\phi')\Delta_{loc}(|\mathbf{r}-\mathbf{r}'|) + \hat{w}(R_{-\phi}(\mathbf{r}-\mathbf{r}'))\Delta_{lat}(\phi-\phi') \\ &= w(\mathbf{r},\phi|\mathbf{r}',\phi') \end{aligned}$$

We have used the identity $\kappa R_{-\phi} = R_{\phi}\kappa$ and the conditions $w_{loc}(-\phi) = w_{loc}(\phi)$, $\Delta_{lat}(-\phi) = \Delta_{lat}(\phi)$, $\hat{w}(\kappa\mathbf{r}) = \hat{w}(\mathbf{r})$.

Implications of Euclidean symmetry Consider the action of γ on equation (2.1) for $h(\mathbf{r},t)=0$:

$$\begin{aligned}\frac{\partial a(\gamma^{-1}P,t)}{\partial t} &= -\alpha a(\gamma^{-1}P,t)+\mu\int_{\mathbf{R}^2\times\mathbf{S}^1} w(\gamma^{-1}P|P')\sigma[a(P',t)]dP' \\ &= -\alpha a(\gamma^{-1}P,t)+\mu\int_{\mathbf{R}^2\times\mathbf{S}^1} w(P|\gamma P')\sigma[a(P',t)]dP' \\ &= -\alpha a(\gamma^{-1}P,t)+\mu\int_{\mathbf{R}^2\times\mathbf{S}^1} w(P|P'')\sigma[a(\gamma^{-1}P'',t)]dP''\end{aligned}$$

since $d[\gamma^{-1}P]=\pm dP$ and w is Euclidean invariant. If we rewrite equation (2.1) as an operator equation, namely,

$$\mathsf{F}[a]\equiv\frac{da}{dt}-\mathsf{G}[a]=0,$$

then it follows that $\gamma\mathsf{F}[a]=\mathsf{F}[\gamma a]$. Thus F commutes with $\gamma\in\mathbf{E}(2)$ and F is said to be equivariant with respect to the symmetry group $\mathbf{E}(2)$ (Golubitsky, Stewart, & Schaeffer, 1988). The equivariance of the operator F with respect to the action of $\mathbf{E}(2)$ has major implications for the nature of solutions bifurcating from the homogeneous resting state. Let μ be a bifurcation parameter. We show in §4 that near a point for which the steady–state $a(\mathbf{r},\phi,\mu)=0$ becomes unstable, there must exist smooth solutions to the equilibrium equation $\mathsf{G}[a(\mathbf{r},\phi,\mu)]=0$ that are identified by their symmetry (Golubitsky *et al.*, 1988). We find solutions that are doubly periodic with respect to a rhombic, square or hexagonal lattice by using the remnants of Euclidean symmetry on these lattices. These remnants are the (semi–direct) products Γ of the torus $\mathbf{T}^2$ of translations modulo the lattice with the dihedral groups $\mathbf{D}_2$, $\mathbf{D}_4$ and $\mathbf{D}_6$, the holohedries of the lattice. Thus, when $a(\mathbf{r},\phi,\mu)=0$ becomes unstable, new solutions emerge from the instability with symmetries that are broken compared with Γ. Sufficiently close to the bifurcation point these patterns are characterized by (finite) linear combinations of eigenfunctions of the linear operator $\mathsf{L}=D_0\mathsf{G}$ obtained by linearizing equation (2.1) about the homogeneous state $a=0$. These eigenfunctions are derived in §3.

2.3 Two limiting cases

For the sake of mathematical convenience, we restrict our analysis in this paper to the simpler weight distribution given by equations (2.3) and (2.4) with $\hat{w}$ satisfying either equation (2.5) or (2.8). The most important property of w is its invariance under the extended Euclidean group action (2.9), which is itself a natural consequence of the anisotropic pattern of lateral connections. Substitution of equation (2.3) into equation (2.1) gives (for zero external inputs)

$$\begin{aligned}\frac{\partial a(\mathbf{r},\phi,t)}{\partial t} &= -\alpha a(\mathbf{r},\phi,t)+\mu\left[\int_0^\pi w_{loc}(\phi-\phi')\sigma[a(\mathbf{r},\phi',t)]\frac{d\phi'}{\pi}\right. \\ &\left.+\beta\int_{\mathbf{R}^2} w_{lat}(\mathbf{r}-\mathbf{r}',\phi)\sigma[a(\mathbf{r}',\phi,t)]d\mathbf{r}'\right]\end{aligned} \tag{2.11}$$

where we have introduced an additional coupling parameter β that characterizes the relative strength of lateral interactions. Equation (2.11) is of convolution type, in that the weighting functions are homogeneous in their respective domains. However, the weighting function $w_{lat}(\mathbf{r},\phi)$ is anisotropic, since it depends on ϕ. Before proceding to analyze the full model described by equation (2.11), it is useful to consider two limiting cases, namely the ring model of orientation tuning and the Ermentrout–Cowan model (Ermentrout & Cowan, 1979).

The Ring model of orientation tuning

The first limiting case is to neglect lateral connections completely by setting $\beta = 0$ in equation (2.11). Each point $\mathbf{r}$ in the cortex is then independently described by the so–called ring model of orientation tuning (Hansel & Sompolinsky, 1997; Mundel, Dimitrov, & Cowan, 1997; Ermentrout, 1998; Bressloff, Bressloff, & Cowan, 2000a):

$$\frac{\partial a(\mathbf{r},\phi,t)}{\partial t} = -\alpha a(\mathbf{r},\phi,t)+\mu\int_0^\pi w_{loc}(\phi-\phi')\sigma[a(\mathbf{r},\phi',t)]\frac{d\phi'}{\pi} \tag{2.12}$$

Linearizing this equation about the homogeneous state $a(\mathbf{r},\phi,t)\equiv 0$ and considering perturbations of the form $a(\mathbf{r},\phi,t)=\mathrm{e}^{\lambda t}a(\mathbf{r},\phi)$ yields the eigenvalue equation

$$\lambda a(\mathbf{r},\phi) = -\alpha a(\mathbf{r},\phi)+\mu\int_0^\pi w_{loc}(\phi-\phi')a(\mathbf{r},\phi')\frac{d\phi'}{\pi}$$

Introducing the Fourier series expansion $a(\mathbf{r},\phi)=\sum_m z_m(\mathbf{r})\mathrm{e}^{2im\phi}+c.c.$ generates the following discrete dispersion relation for the eigenvalue λ:

$$\lambda=-\alpha+\sigma_1\mu W_m\equiv\lambda_m \tag{2.13}$$

where $\sigma_1=d\sigma[z]/dz$ evaluated at $z=0$ and

$$w_{loc}(\phi)=\sum_{n\in\mathbf{Z}}W_n\mathrm{e}^{2ni\phi} \tag{2.14}$$

Note that since $w_{loc}(\phi)$ is a real and even function of ϕ, $W_{-m}=W_m=\overline{W}_m$.

Let $W_p=\max\{W_n,n\in\mathbf{Z}^+\}$ and suppose that p is unique with $W_p>0$ and $p\geq 1$. It then follows from equation (2.13) that the homogeneous state $a(\mathbf{r},\phi)=0$ is stable for sufficiently small μ, but becomes unstable when μ increases beyond the critical value $\mu_c=\alpha/\sigma_1 W_p$ due to excitation of linear eigenmodes of the form $a(\mathbf{r},\phi)=z(\mathbf{r})\mathrm{e}^{2ip\phi}+\overline{z}(\mathbf{r})\mathrm{e}^{-2ip\phi}$, where $z(\mathbf{r})$ is an arbitrary complex function of $\mathbf{r}$. It can be shown that the saturating nonlinearities of the system stabilize the growing pattern of activity (Ermentrout, 1998; Bressloff *et al.*, 2000a). In terms of polar coordinates $z(\mathbf{r})=Z(\mathbf{r})\mathrm{e}^{2i\phi(\mathbf{r})}$ we have $a(\mathbf{r},\phi)=Z(\mathbf{r})\cos(2p[\phi-\phi(\mathbf{r})])$. Thus at each point $\mathbf{r}$ in the plane the maximum (linear) response occurs at the orientations $\phi(\mathbf{r})+k\pi/p$, $k=0,1,\ldots,p-1$ when $p\neq 0$.

Of particular relevance from a biological perspective are the cases $p=0$ and $p=1$. In the first case there is a bulk instability in which the new steady state shows no orientation preference. Any tuning is generated in the genico–cortical map. We call this the 'Hubel–Wiesel' mode (Hubel & Wiesel, 1974a). In the second case the response is unimodal with respect to ϕ. The occurrence of a sharply tuned response peaked at some angle $\phi(\mathbf{r})$ in a local region of V1 corresponds to the presence of a local contour there, whose orientation is determined by the inverse of the double retino–cortical map described in §5.1. An example of a typical unimodal tuning curve is shown in figure 14, which is obtained by taking $w_{loc}(\phi)$ to be a difference–of–Gaussians over the domain $[-\pi/2,\pi/2)$:

$$w_{loc}(\phi)=[2\pi\xi_{loc}^2]^{-1/2}\mathrm{e}^{-\phi^2/2\xi_{loc}^2}-A_{loc}[2\pi\hat{\xi}_{loc}^2]^{-1/2}\mathrm{e}^{-\phi^2/2\hat{\xi}_{loc}^2} \tag{2.15}$$

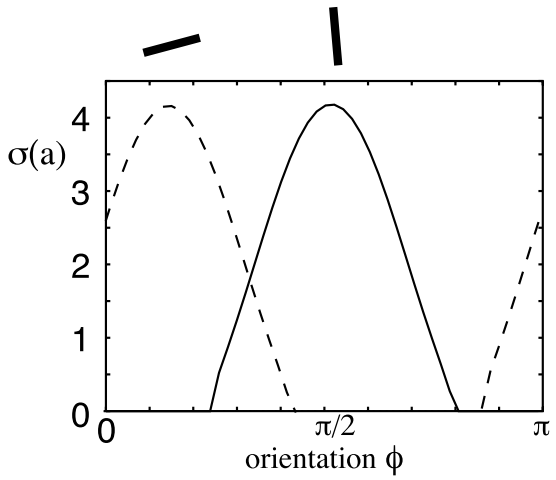

Figure 14: Sharp orientation tuning curves for a Mexican hat weight kernel with $\xi_{loc} = 20^o$, $\hat{\xi}_{loc} = 60^o$ and $A_{loc} = 1$. The tuning curve is marginally stable so that the peak activity a at each point in the cortical plane is arbitrary. The activity is truncated at $\sigma = 0$ in line with the choice of $\sigma[0] = 0$.

with $\xi_{loc} < \hat{\xi}_{loc}$ and $A_{loc} \leq 1$.

The location of the center $\phi(\mathbf{r})$ of each tuning curve is arbitrary, which reflects the rotational equivariance of equation (2.12) under the modified group action $\theta : (\mathbf{r}, \phi) \to (\mathbf{r}, \phi+\theta)$. Moreover, in the absence of lateral interactions the tuned response is uncorrelated across different points in V1. In this paper we show how the presence of anisotropic lateral connections leads to periodic patterns of activity across V1 in which the peaks of the tuning curve at different locations are correlated.

The Ermentrout–Cowan model

The other limiting case is to neglect the orientation label completely. Equation (2.11) then reduces to a one-population version of the model studied by Ermentrout & Cowan (1979):

$$\frac{\partial}{\partial t}a(\mathbf{r},t) = -\alpha a(\mathbf{r},t) + \nu \int_{\Omega} w_{lat}(\mathbf{r}-\mathbf{r}')\sigma\left[a(\mathbf{r}',t)\right] d\mathbf{r}' \tag{2.16}$$

In this model there is no reason to distinguish any direction in V1, so we assume that $w_{lat}(\mathbf{r}-\mathbf{r}') \to w_{lat}(|\mathbf{r}-\mathbf{r}'|)$, i.e. w_{lat} depends only on the magnitude of $\mathbf{r}-\mathbf{r}'$. It can be shown that the resulting system is equivariant with respect to the standard action of the Euclidean group in the plane.

Linearizing equation (2.16) about the homogeneous state and taking $a(\mathbf{r},t) = \mathrm{e}^{\lambda t}a(\mathbf{r})$ gives rise to the eigenvalue problem

$$\lambda a(\mathbf{r}) = -\alpha a(\mathbf{r}) + \nu\sigma_1 \int_{\Omega} w_{lat}(|\mathbf{r}-\mathbf{r}'|)a(\mathbf{r}')d\mathbf{r}',$$

which upon Fourier transforming generates a *dispersion relation* for the eigenvalue λ as a function of $q = |\mathbf{k}|$, i.e.

$$\lambda = -\alpha + \nu\sigma_1\widetilde{W}(q) \equiv \lambda(q)$$

where $\widetilde{W}(q) = \widetilde{w}_{lat}(\mathbf{k})$ is the Fourier transform of $w_{lat}(|\mathbf{r}|)$. Note that λ is real. If we choose $w_{lat}(|\mathbf{r}|)$ to be in the form of a Mexican hat function, then it is simple to establish that λ passes through zero at a critical parameter value ν_c signalling the growth of

spatially periodic patterns with wavenumber q_c, where $\widetilde{W}(q_c) = \max_q\{\widetilde{W}(q)\}$. Close to the bifurcation point these patterns can be represented as linear combinations of plane waves

$$a(\mathbf{r}) = \sum_i c_i \mathrm{e}^{i\mathbf{k}_i\cdot\mathbf{r}}$$

with $|\mathbf{k}_i| = q_c$. As shown in Ermentrout & Cowan (1979) and Cowan (1982), the underlying Euclidean symmetry of the weighting function together with the restriction to doubly periodic functions then determines the allowable combinations of plane waves comprising steady state solutions. In particular, stripe, checkerboard and hexagonal patterns of activity can form in the V1 map of the visual field. In this paper we generalize the treatment by Ermentrout & Cowan to incorporate the effects of orientation preference—and show how plane waves of cortical activity modulate the distribution of tuning curves across the network and lead to contoured patterns.

3 Linear stability analysis

The first step in the analysis of pattern forming instabilities in the full cortical model is to linearize equation (2.11) about the homogeneous solution $a(\mathbf{r}, \phi) = 0$ and to solve the resulting eigenvalue problem. In particular, we wish to find conditions under which the homogeneous solution becomes marginally stable due to the vanishing of one of the (degenerate) eigenvalues, and to identify the marginally stable modes. This will require performing a perturbation expansion with respect to the small parameter β characterizing the relative strength of the anisotropic lateral connections.

3.1 Linearization

We linearize equation (2.11) about the homogeneous state and introduce solutions of the form $a(\mathbf{r},\phi,t) = \mathrm{e}^{\lambda t}a(\mathbf{r},\phi)$. This generates the eigenvalue equation

$$\begin{aligned}\lambda a(\mathbf{r},\phi) &= -\alpha a(\mathbf{r},\phi) + \sigma_1\mu\left[\int_0^\pi w_{loc}(\phi-\phi')a(\mathbf{r},\phi')\frac{d\phi'}{\pi}\right.\\ &\left.+\beta\int_{\mathbf{R}^2} w_{lat}(\mathbf{r}-\mathbf{r}',\phi)a(\mathbf{r}',\phi)d\mathbf{r}'\right] \qquad (3.1)\end{aligned}$$

Because of translation symmetry, the eigenvalue equation (3.1) can be written in the form

$$a(\mathbf{r},\phi) = u(\phi-\varphi)e^{i\mathbf{k}\cdot\mathbf{r}} + c.c. \qquad (3.2)$$

with $\mathbf{k} = q(\cos\varphi,\sin\varphi)$ and

$$\lambda u(\phi) = -\alpha u(\phi) + \sigma_1\mu\left[\int_0^\pi w_{loc}(\phi-\phi')u(\phi')\frac{d\phi'}{\pi} + \beta\widetilde{w}_{lat}(\mathbf{k},\phi+\varphi)u(\phi)\right] \qquad (3.3)$$

Here $\widetilde{w}_{lat}(\mathbf{k},\phi)$ is the Fourier transform of $w_{lat}(\mathbf{r},\phi)$.

Assume that w_{lat} satisfies equations (2.4) and (2.5) so that the total weight distribution w is Euclidean invariant. The resulting symmetry of the system then restricts the structure of the solutions of the eigenvalue equation (3.3):

(i) λ and $u(\phi)$ only depend on the magnitude $q = |\mathbf{k}|$ of the wave vector $\mathbf{k}$. That is, there is an infinite degeneracy due to rotational invariance.

(ii) For each $\mathbf{k}$ the associated subspace of eigenfunctions

$$V_{\mathbf{k}} = \{u(\phi-\varphi)\mathrm{e}^{i\mathbf{k}\cdot\mathbf{r}} + c.c \ : \ u(\phi+\pi) = u(\phi) \quad \text{and} \quad u\in\mathbf{C}\} \qquad (3.4)$$

decomposes into two invariant subspaces

$$V_{\mathbf{k}} = V_{\mathbf{k}}^+ \oplus V_{\mathbf{k}}^-, \qquad (3.5)$$

corresponding to even and odd functions respectively

$$V_{\mathbf{k}}^+ = \{v\in V_{\mathbf{k}} : u(-\phi) = u(\phi)\} \quad \text{and} \quad V_{\mathbf{k}}^- = \{v\in V_{\mathbf{k}} : u(-\phi) = -u(\phi)\}. \qquad (3.6)$$

As noted in greater generality by Bosch Vivancos, Chossat, & Melbourne (1995), this is a consequence of reflection invariance, as we now indicate. That is, let $\kappa_{\mathbf{k}}$ denote reflections about the wavevector $\mathbf{k}$ so that $\kappa_{\mathbf{k}}\mathbf{k} = \mathbf{k}$. Then $\kappa_{\mathbf{k}} a(\mathbf{r}, \phi) = a(\kappa_{\mathbf{k}}\mathbf{r}, 2\varphi - \phi) = u(\varphi - \phi)\mathrm{e}^{i\mathbf{k}\cdot\mathbf{r}} + c.c.$ Since $\kappa_{\mathbf{k}}$ is a reflection, any space that it acts on decomposes into two subspaces – one on which it acts as the identity I and one on which it acts as $-I$.

Results (i) and (ii) can also be derived directly from equation (3.3). For expanding the π-periodic function $u(\phi)$ as a Fourier series with respect to ϕ

$$u(\phi) = \sum_{n\in\mathbf{Z}} A_n \mathrm{e}^{2ni\phi} \tag{3.7}$$

and setting $w_{lat}(\mathbf{r}, \phi) = \hat{w}(R_{-\phi}\mathbf{r})$ leads to the matrix eigenvalue equation

$$\lambda A_m = -\alpha A_m + \sigma_1 \mu \left[W_m A_m + \beta \sum_{n\in\mathbf{Z}} \hat{W}_{m-n}(q) A_n \right] \tag{3.8}$$

with W_n given by equation (2.14) and

$$\hat{W}_n(q) = \int_0^\pi \mathrm{e}^{-2in\phi} \left[\int_{\mathbf{R}^2} \mathrm{e}^{-iq[x\cos(\phi)+y\sin(\phi)]} \hat{w}(\mathbf{r}) d\mathbf{r} \right] \frac{d\phi}{\pi} \tag{3.9}$$

It is clear from equation (3.8) that item (i) holds. The decomposition of the eigenfunctions into odd and even invariant subspaces, see equation (3.5) of item (ii), is a consequence of the fact that $\hat{w}(\mathbf{r})$ is an even function of x and y, see equation (2.5), and hence $\hat{W}_n(q) = \hat{W}_{-n}(q)$.

3.2 Eigenfunctions and Eigenvalues

The calculation of the eigenvalues and eigenfunctions of the linearized equation (3.1), and hence the derivation of conditions for the marginal stability of the homogeneous state, has been reduced to the problem of solving the matrix equation (3.8), which we rewrite in the more convenient form

$$\left[\frac{\lambda + \alpha}{\sigma_1 \mu} - W_m \right] A_m = \beta \sum_{n\in\mathbf{Z}} \hat{W}_{m-n}(q) A_n \tag{3.10}$$

We exploit the experimental observation that the intrinsic lateral connections appear to be weak relative to the local connections, i.e. $\beta\hat{W} \ll W$. Equation (3.10) can then be solved by expanding as a power series in β and using Rayleigh–Schrödinger perturbation theory.

Case $\beta = 0$ In the limiting case of zero lateral interactions equation (3.10) reduces to (2.13). Following the discussion of the ring model in §2.3, let $W_p = \max\{W_n, n \in \mathbf{Z}^+\} > 0$ and suppose that $p = 1$ (unimodal orientation tuning curves). The homogeneous state $a(\mathbf{r}, \phi) = 0$ is then stable for sufficiently small μ, but becomes marginally stable at the critical point $\mu_c = \alpha/\sigma_1 W_1$ due to the vanishing of the eigenvalue λ_1. In this case there are both even and odd marginally stable modes $\cos(2\phi)$ and $\sin(2\phi)$.

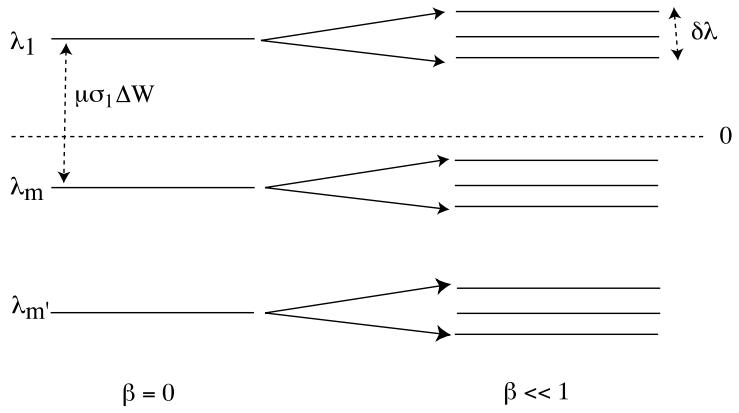

Figure 15: Splitting of degenerate eigenvalues due to anisotropic lateral connections between hypercolumns.

Case $\beta > 0$ If we now switch on the lateral connections, then there is a q–dependent *splitting* of the degenerate eigenvalue λ_1 that also separates out odd and even solutions. Denoting the characteristic size of such a splitting by $\delta\lambda = \mathcal{O}(\beta)$, we impose the condition that $\delta\lambda \ll \mu\sigma_1\Delta W$, where

$$\Delta W = \min\{W_1 - W_m, m \neq 1\}.$$

This ensures that the perturbation does not excite states associated with other eigenvalues of the unperturbed problem, see figure 15. We can then restrict ourselves to calculating perturbative corrections to the degenerate eigenvalue λ_1 and its associated eigenfunctions. Therefore, introduce the power series expansions

$$\frac{\lambda+\alpha}{\sigma_1\mu} = W_1 + \beta\lambda^{(1)} + \beta^2\lambda^{(2)} + \dots \tag{3.11}$$

and

$$A_n = z_{\pm 1}\delta_{n,\pm 1} + \beta A_n^{(1)} + \beta^2 A_n^{(2)} + \dots \tag{3.12}$$

where $\delta_{n,m}$ is the Kronecker delta function. Substitute these expansions into the matrix eigenvalue equation (3.10) and systematically solve the resulting hierarchy of equations to successive orders in β using (degenerate) perturbation theory. This analysis, which is carried out in appendix A.1, leads to the following results: (i) $\lambda = \lambda_\pm$ for even (+) and odd (−) solutions where to $\mathcal{O}(\beta^2)$

$$\begin{aligned}\frac{\lambda_\pm+\alpha}{\sigma_1\mu} &= W_1 + \beta\left[\hat{W}_0(q) \pm \hat{W}_2(q)\right] + \beta^2 \sum_{m\geq 0, m\neq 1} \frac{\left[\hat{W}_{m-1}(q) \pm \hat{W}_{m+1}(q)\right]^2}{W_1 - W_m} \\ &\equiv G_\pm(q)\end{aligned} \tag{3.13}$$

and (ii) $u(\phi) = u_\pm(\phi)$ where to $\mathcal{O}(\beta)$

$$u_+(\phi) = \cos(2\phi) + \beta \sum_{m\geq 0, m\neq 1} u_m^+(q)\cos(2m\phi) \tag{3.14}$$

$$u_-(\phi) = \sin(2\phi) + \beta \sum_{m>1} u_m^-(q)\sin(2m\phi) \tag{3.15}$$

with

$$u_0^+(q) = \frac{\hat{W}_1(q)}{W_1 - W_0}, \qquad u_m^\pm(q) = \frac{\hat{W}_{m-1}(q) \pm \hat{W}_{m+1}(q)}{W_1 - W_m},\ m > 1 \tag{3.16}$$

3.3 Marginal stability

Suppose that $G_{\pm}(q)$ has a unique maximum at $q = q_{\pm} \neq 0$ and let $q_c = q_+$ if $G_+(q_+) > G_-(q_-)$ and $q_c = q_-$ if $G_-(q_-) > G_+(q_+)$. Under such circumstances, the homogeneous state $a(\mathbf{r}, \phi) = 0$ will become marginally stable at the critical point $\mu_c = \alpha/\sigma_1 G_{\pm}(q_c)$ and the marginally stable modes will be of the form

$$a(\mathbf{r}, \phi) = \sum_{i=1}^{N} c_i \mathrm{e}^{i\mathbf{k}_i \cdot \mathbf{r}} u(\phi - \varphi_i) + c.c. \tag{3.17}$$

where $\mathbf{k}_i = q_c(\cos\varphi_i, \sin\varphi_i)$ and $u(\phi) = u_{\pm}(\phi)$ for $q_c = q_{\pm}$. The infinite degeneracy arising from rotation invariance means that all modes lying on the circle $|\mathbf{k}| = q_c$ become marginally stable at the critical point. However, this can be reduced to a finite set of modes by restricting solutions to be doubly periodic functions. The types of doubly periodic solutions that can bifurcate from the homogeneous state will be determined in §4.

As a specific example illustrating marginal stability let $\hat{w}(\mathbf{r})$ be given by equation (2.5). Substitution into equation (3.9) gives

$$\hat{W}_n(q) = \int_0^{\pi} \mathrm{e}^{-2in\phi} \left[\int_0^{\infty} g(s) \cos(sq\cos\phi) ds \right] \frac{d\phi}{\pi}$$

Using the Jacobi-Anger expansion

$$\cos(sq\cos\phi) = J_0(sq) + 2\sum_{m=1}^{\infty} (-1)^m J_{2m}(sq)\cos(2m\phi)$$

with $J_n(x)$ the Bessel function of integer order n, we derive the result

$$\hat{W}_n(q) = (-1)^n \int_0^{\infty} g(s) J_{2n}(sq) ds \tag{3.18}$$

Next substitute equation (2.6) into (3.18) and use standard properties of Bessel functions to obtain

$$\hat{W}_n(q) = \frac{(-1)^n}{2} \left[\mathrm{e}^{-\xi_{lat}^2 q^2/4} I_n(\xi_{lat}^2 q^2/4) - A_{lat} \mathrm{e}^{-\hat{\xi}_{lat}^2 q^2/4} I_n(\hat{\xi}_{lat}^2 q^2/4) \right] \tag{3.19}$$

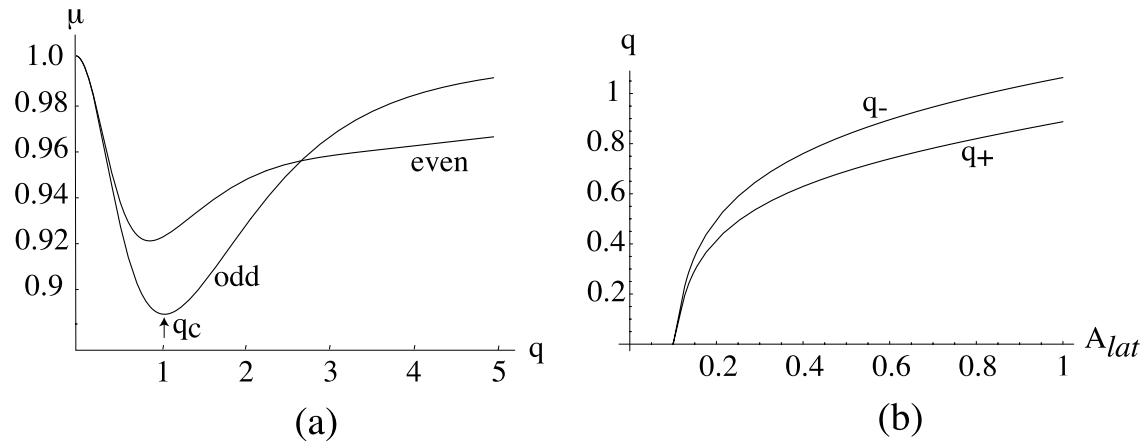

Figure 16: (a) Plot of marginal stability curves $\mu_{\pm}(q)$ for $g(s)$ given by the difference–of–Gaussians (2.6) with $\xi_{lat} = 1$, $\hat{\xi}_{lat} = 3$, $A_{lat} = 1$ and $\beta = 0.4W_1$. Also set $\alpha/\sigma_1 W_1 = 1$. The critical wavenumber for spontaneous pattern formation is q_c. The marginally stable eigenmodes are odd functions of ϕ. (b) Plot of critical wavenumber $q_{\pm}$ for marginal stability of even (+) and odd (−) patterns as a function of the strength of inhibitory coupling A_{lat}. If the inhibition is too weak then there is a bulk instability with respect to the spatial domain.

where I_n is a modified Bessel function of integer order n. The resulting marginal stability curves $\mu = \mu_{\pm}(q) = \alpha/\sigma_1 G_{\pm}(q)$ are plotted to first order in β in figure 16(a). The existence of a non–zero critical wavenumber $q_c = q_-$ at $\mu_c = \mu_-(q_c)$ is evident, indicating that the marginally stable eigenmodes are odd functions of ϕ. The inclusion of higher–order terms in β does not alter this basic result, at least for small β. If we take the fundamental unit of length to be about 400 μm then the wavelength of a pattern is $2\pi(0.400)/q_c$ mm, about 2.66 mm at the critical wavenumber $q_c = 1$ (see figure 16(b)).

An interesting question concerns under what circumstances can even patterns be excited by a primary instability rather than odd, in the regime of weak lateral interactions. One example occurs when there is a sufficient spread in the distribution of lateral connections along the lines shown in figure 12. In particular, suppose that $\hat{w}(\mathbf{r})$ is given by equation (2.8) with $p(\theta) = 1$ for $\theta \leq \theta_0$ and zero otherwise. Equation

(3.18) then becomes

$$\hat{W}_n(q) = (-1)^n \frac{\sin(2n\theta_0)}{2n\theta_0} \int_0^\infty g(s) J_{2n}(sq) ds \tag{3.20}$$

To first order in β the size of the gap between the odd and even eigenmodes at the critical point q_c is determined by $2\hat{W}_2(q_c)$, see equation (3.13). It follows that if $\theta_0 > \pi/4$ then $\hat{W}_2(q)$ reverses sign suggesting that even rather than odd eigenmodes become marginally stable first. This is confirmed by the marginal stability curves shown in figure 17.

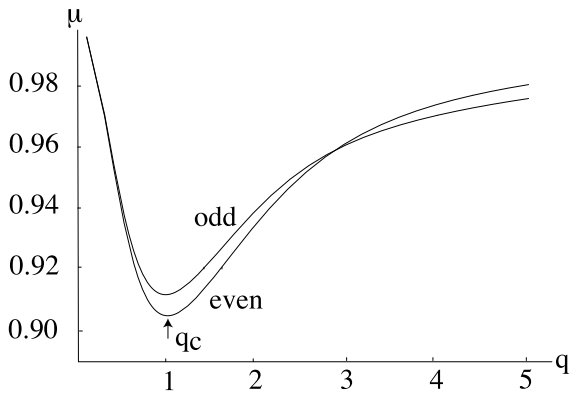

Figure 17: Same as figure 16 except that $\hat{W}(q)$ satisfies equation (3.20) with $\theta_0 = \pi/3$ rather than (3.18). It can be seen that the marginally stable eigenmodes are now even functions of ϕ.

Choosing the bifurcation parameter

It is worth commenting at this stage on the choice of bifurcation parameter μ. One way to induce a primary instability of the homogeneous state is to increase the global coupling parameter μ in equation (3.13) until the critical point μ_c is reached. However, it is clear from equation (3.13) that an equivalent way to induce such an instability is to keep μ fixed and increase the slope σ_1 of the neural output function σ. The latter could be achieved by keeping a non-zero uniform input $h(\mathbf{r}, \phi, t) = h_0$ in equation (2.1)

so that the homogeneous state is non-zero, $a(\mathbf{r}, \phi, t) = a_0 \neq 0$ with $\sigma_1 = \sigma'(a_0)$. Then variation of the input h_0 and consequently σ_1, corresponds to changing the effective neural threshold and hence the level of network excitability. Indeed, this is thought to be one of the possible effects of hallucinogens. In summary, the mathematically convenient choice of μ as the bifurcation parameter can be reinterpreted in terms of biologically meaningful parameter variations. It is also possible that hallucinogens act indirectly on the relative levels of inhibition and this could also play a role in determining the type of patterns that emerge—a particular example is discussed below.

3.4 The Ermentrout–Cowan model revisited

The marginally stable eigenmodes (3.17) identified in the analysis consist of spatially periodic patterns of activity that modulate the distribution of orientation tuning curves across V1. Examples of these contoured cortical planforms will be presented in §4 and the corresponding hallucination patterns in the visual field (obtained by applying an inverse retino–cortical map) will be constructed in §5. It turns out that the resulting patterns account for some of the more complicated form constants where contours are prominent, including cobwebs, honeycombs and lattices (figure 4). However, other form constants such as checkerboards, funnels and spirals (figures 6 and 7) comprise contrasting regions of light and dark. One possibility is that these hallucinations are a result of higher level processes filling in the contoured patterns generated in V1. An alternative explanation is that such regions are actually formed in V1 itself by a mechanism similar to that suggested in the original Ermentrout–Cowan model. This raises the interesting issue as to whether or not there is some parameter regime in which the new model can behave in a similar fashion to the 'cortical retina' of Ermentrout–Cowan, that is, can cortical orientation tuning somehow be switched off? One possible mechanism is the following: suppose that the relative level of local inhibition, which is specified by the parameter A_{loc} in equation (2.15), is reduced (e.g., by the possible (indirect) action of hallucinogens.) Then $W_0 = \max\{W_n, n \in \mathbf{Z}^+\}$ rather than W_1, and the marginally stable eigenmodes will consist of spatially periodic

patterns that modulate bulk instabilitities with respect to orientation.

To make these ideas more explicit, we introduce the perturbation expansions

$$\frac{\lambda+\alpha}{\sigma_1\mu} = W_0 + \beta\lambda^{(1)} + \beta^2\lambda^{(2)} + \dots \tag{3.21}$$

and

$$A_n = z\delta_{n,0} + \beta A_n^{(1)} + \beta^2 A_n^{(2)} + \dots \tag{3.22}$$

Substituting these expansions into the matrix eigenvalue equation (3.10) and solving the resulting equations to successive orders in β leads to the following results:

$$\begin{aligned} \frac{\lambda+\alpha}{\sigma_1\mu} &= W_0 + \beta\hat{W}_0(q) + \beta^2 \sum_{m>0} \frac{\hat{W}_m(q)^2}{W_0 - W_m} + \mathcal{O}(\beta^3) \\ &\equiv G_0(q) \end{aligned} \tag{3.23}$$

and

$$u(\phi) = 1 + \beta \sum_{m>0} u_m^0(q)\cos(2m\phi) + \mathcal{O}(\beta^2) \tag{3.24}$$

with

$$u_m^0(q) = \frac{\hat{W}_m(q)}{W_0 - W_m} \tag{3.25}$$

Substituting equation (3.24) into (3.17) shows that the marginally stable states are now only weakly dependent on the orientation ϕ, and to lowest order in β simply correspond to the spatially periodic patterns of the Ermentrout–Cowan model. The length–scale of these patterns is determined by the marginal stability curve $\mu_0(q) = \alpha/\sigma_1 G_0(q)$, an example of which is shown in figure 18.

The occurrence of a bulk instability in orientation means that for sufficiently small β the resulting cortical patterns will be more like contrasting regions of light and dark rather than a lattice of oriented contours (see §4). However, if the strength of lateral connections β were increased then the eigenfunctions (3.24) would develop a significant dependence on the orientation ϕ. This could then provide an alternative mechanism for the generation of even contoured patterns—recall from §3.3 that only odd contoured patterns emerge in the case of a tuned instability with respect to orientation, unless there is significant angular spread in the lateral connections.

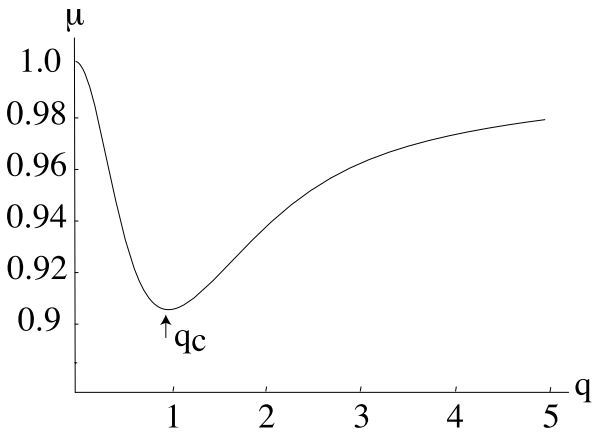

Figure 18: Plot of marginal stability curve $\mu_0(q)$ for a bulk instability with respect to orientation and $g(s)$ given by the difference–of–Gaussians (2.6) with $\xi_{lat} = 1$, $\hat{\xi}_{lat} = 3$, $A_{lat} = 1.0$, $\beta = 0.4W_0$ and $\alpha/\sigma_1 W_0 = 1$. The critical wavenumber for spontaneous pattern formation is q_c.

4 Doubly–periodic planforms

As we found in §3.3 and §3.4, rotation symmetry implies that the space of marginally stable eigenfunctions of the linearized Wilson–Cowan equation is infinite–dimensional, that is, if $u(\phi)\mathrm{e}^{i\mathbf{k}\cdot\mathbf{r}}$ is a solution then so is $u(\phi-\varphi)\mathrm{e}^{iR_\varphi\mathbf{k}\cdot\mathbf{r}}$. However, translation symmetry suggests that we can restrict the space of solutions of the nonlinear Wilson–Cowan equation (2.11) to that of doubly–periodic functions. This restriction is standard in many treatments of spontaneous pattern formation, but as yet it has no formal justification. There is however a wealth of evidence from experiments on convecting fluids and chemical reaction-diffusion systems (Walgraef, 1997), and simulations of neural nets (von der Malsburg & Cowan, 1982), which indicates that such systems tend to generate doubly–periodic patterns in the plane, when the homogeneous state is destabilized. Given such a restriction the associated space of marginally stable eigenfunctions is then finite–dimensional. A finite set of specific eigenfunctions can then be identified as candidate planforms in the sense that they approximate time–

independent solutions of equation (2.11) sufficiently close to the critical point where the homogeneous state loses stability. In this section we construct such planforms.

4.1 Restriction to doubly periodic solutions

Let $\mathcal{L}$ be a planar lattice; that is, choose two linearly independent vectors $\boldsymbol{\ell}_1$ and $\boldsymbol{\ell}_2$ and let

$$\mathcal{L} = \{2\pi m_1 \boldsymbol{\ell}_1 + 2\pi m_2 \boldsymbol{\ell}_2 : m_1, m_2 \in \mathbf{Z}\}.$$

Note that $\mathcal{L}$ is a subgroup of the group of planar translations. A function $f : \mathbf{R}^2 \times \mathbf{S}^1 \to \mathbf{R}$ is doubly periodic with respect to $\mathcal{L}$ if

$$f(x + \boldsymbol{\ell}, \phi) = f(x, \phi)$$

for every $\boldsymbol{\ell} \in \mathcal{L}$. Let θ be the angle between the two basis vectors $\boldsymbol{\ell}_1$ and $\boldsymbol{\ell}_2$. We can then distinguish three types of lattice according to the value of θ: square lattice ($\theta = \pi/2$), rhombic lattice ($0 < \theta < \pi/2$, $\theta \neq \pi/3$) and hexagonal ($\theta = \pi/3$). After rotation, the generators of the planar lattices are given in Table 1 (for unit lattice spacing).

Lattice	$\boldsymbol{\ell}_1$	$\boldsymbol{\ell}_2$	$\mathbf{k}_1$	$\mathbf{k}_2$
Square	$(1, 0)$	$(0, 1)$	$(1, 0)$	$(0, 1)$
Hexagonal	$(1, \frac{1}{\sqrt{3}})$	$(0, \frac{2}{\sqrt{3}})$	$(1, 0)$	$\frac{1}{2}(-1, \sqrt{3})$
Rhombic	$(1, -\cot\eta)$	$(0, \csc\eta)$	$(1, 0)$	$(\cos\eta, \sin\eta)$

Table 1: Generators for the planar lattices and their dual lattices.

Restriction to double periodicity means that the original Euclidean symmetry group is now restricted to the symmetry group of the lattice, $\Gamma_{\mathcal{L}} = H_{\mathcal{L}} \dot{+} \mathbf{T}^2$, where $H_{\mathcal{L}}$ is the holohedry of the lattice, the subgroup of $\mathbf{O}(2)$ that preserves the lattice, and $\mathbf{T}^2$ is the two torus of planar translations modulo the lattice. Thus, the holohedry of the rhombic lattice is $\mathbf{D}_2$, the holohedry of the square lattice is $\mathbf{D}_4$ and the holohedry

of the hexagonal lattice is $\mathbf{D}_6$. Observe that the corresponding space of marginally stable modes is now finite–dimensional—we can only rotate eigenfunctions through a finite set of angles (for example, multiples of $\pi/2$ for the square lattice and multiples of $\pi/3$ for the hexagonal lattice).

It remains to determine the space $K_{\mathcal{L}}$ of marginally stable eigenfunctions and the action of $\Gamma_{\mathcal{L}}$ on this space. In §3 we showed that eigenfunctions either reside in $V_{\mathbf{k}}^{+}$ (the even case) or $V_{\mathbf{k}}^{-}$ (the odd case) where the length of $\mathbf{k}$ is equal to the critical wavenumber q_c. In particular the eigenfunctions have the form $u(\phi-\varphi)\mathrm{e}^{i\mathbf{k}\cdot\mathbf{r}}$ where u is either an odd or even eigenfunction. We now choose the size of the lattice so that $\mathrm{e}^{i\mathbf{k}\cdot\mathbf{r}}$ is doubly periodic with respect to that lattice, that is, $\mathbf{k}$ is a dual wave vector for the lattice. In fact, there are infinitely many choices for the lattice size that satisfies this constraint—we select the one for which q_c is the shortest length of a dual wave vector. The generators for the dual lattices are also given in Table 1 with $q_c = 1$. The eigenfunctions corresponding to dual wave vectors of unit length are given in Table 2. It follows that $K_{\mathcal{L}}$ can be identified with the m–dimensional complex vector space spanned by the vectors $(c_1,\ldots,c_m) \in \mathbf{C}^m$ with $m = 2$ for square or rhombic lattices and $m = 3$ for hexagonal lattices. It can be shown that these form $\Gamma_{\mathcal{L}}$-irreducible representations. The actions of the group $\Gamma_{\mathcal{L}}$ on $K_{\mathcal{L}}$ can then be explicitly written down for both the square or rhombic and hexagonal lattices in both the odd and even cases. These actions are given in appendix A.2.

Lattice	$a(\mathbf{r},\phi)$
Square	$c_1 u(\phi)e^{i\mathbf{k}_1\cdot\mathbf{r}} + c_2 u(\phi-\frac{\pi}{2})e^{i\mathbf{k}_2\cdot\mathbf{r}} + c.c.$
Hexagonal	$c_1 u(\phi)e^{i\mathbf{k}_1\cdot\mathbf{r}} + c_2 u(\phi-\frac{2\pi}{3})e^{i\mathbf{k}_2\cdot\mathbf{r}} + c_3 u(\phi+\frac{2\pi}{3})e^{i\mathbf{k}_3\cdot\mathbf{r}} + c.c.$
Rhombic	$c_1 u(\phi)e^{i\mathbf{k}_1\cdot\mathbf{r}} + c_2 u(\phi-\eta)e^{i\mathbf{k}_2\cdot\mathbf{r}} + c.c.$

Table 2: Eigenfunctions corresponding to shortest dual wave vectors.

4.2 Planforms

We now use an important result from bifurcation theory in the presence of symmetries, namely, the equivariant branching lemma (Golubitsky *et al.*, 1988). For our particular problem, the equivariant branching lemma implies that generically there exists a (unique) doubly periodic solution bifurcating from the homogeneous state for each of the axial subgroups of $\Gamma_{\mathcal{L}}$ under the action (2.9)—a subgroup $\Sigma \subset \Gamma_{\mathcal{L}}$ is axial if the dimension of the space of vectors that are fixed by Σ is equal to one. The axial subgroups are calculated from the actions presented in appendix A.2 (see Bressloff, Cowan, Golubitsky, & Thomas (2000b) for details) and lead to the even planforms listed in Table 3 and the odd planforms listed in Table 4. The generic planforms can then be generated by combining basic properties of the Euclidean group action (2.9) on doubly periodic functions with solutions of the underlying linear eigenvalue problem. The latter determines both the critical wavenumber q_c and the π–periodic function $u(\phi)$. In particular, the perturbation analysis of §3.3 and §3.4 shows that (in the case of weak lateral interactions) $u(\phi)$ can take one of three possible forms:

i) even contoured planforms (3.14) with $u(\phi) \approx \cos(2\phi)$

ii) odd contoured planforms (3.15) with $u(\phi) \approx \sin(2\phi)$.

iii) even non–contoured planforms (3.24) with $u(\phi) \approx 1$

Each planform is an approximate steady–state solution $a(\mathbf{r}, \phi)$ of the continuum model (2.11) defined on the unbounded domain $\mathbf{R}^2 \times \mathbf{S}^1$. To determine how these solutions generate hallucinations in the visual field, we first need to interpret the planforms in terms of activity patterns in a bounded domain of V1, which we denote by $\mathcal{M} \subset \mathbf{R}$. Once this has been achieved, the resulting patterns in the visual field can be obtained by applying the inverse retino–cortical map as described in §5.1.

The interpretation of non–contoured planforms is relatively straightforward, since to lowest order in β the solutions are ϕ–independent and can thus be directly treated as activity patterns $a(\mathbf{r})$ in V1 with $\mathbf{r} \in \mathcal{M}$. At the simplest level such patterns can be represented as contrasting regions of light and dark depending on whether $a(\mathbf{r}) > 0$

Lattice	Name	Planform Eigenfunction
square	even square	$u(\phi)\cos x + u\left(\phi - \frac{\pi}{2}\right)\cos y$
	even roll	$u(\phi)\cos x$
rhombic	even rhombic	$u(\phi)\cos(\mathbf{k}_1\cdot\mathbf{r}) + u(\phi-\eta)\cos(\mathbf{k}_2\cdot\mathbf{r})$
	even roll	$u(\phi)\cos(\mathbf{k}_1\cdot\mathbf{r})$
hexagonal	even hexagon (0)	$u(\phi)\cos(\mathbf{k}_1\cdot\mathbf{r}) + u\left(\phi+\frac{\pi}{3}\right)\cos(\mathbf{k}_2\cdot\mathbf{r}) + u\left(\phi-\frac{\pi}{3}\right)\cos(\mathbf{k}_3\cdot\mathbf{r})$
	even hexagon (π)	$u(\phi)\cos(\mathbf{k}_1\cdot\mathbf{r}) + u\left(\phi+\frac{\pi}{3}\right)\cos(\mathbf{k}_2\cdot\mathbf{r}) - u\left(\phi-\frac{\pi}{3}\right)\cos(\mathbf{k}_3\cdot\mathbf{r})$
	even roll	$u(\phi)\cos(\mathbf{k}_1\cdot\mathbf{r})$

Table 3: Even planforms with $u(-\phi) = u(\phi)$. The hexagon solutions (0) and (π) have the same isotropy subgroup, but they are not conjugate solutions.

or $a(\mathbf{r}) < 0$. These regions form square, triangular, or rhombic cells that tile $\mathcal{M}$ as illustrated in figures 19 and 20.

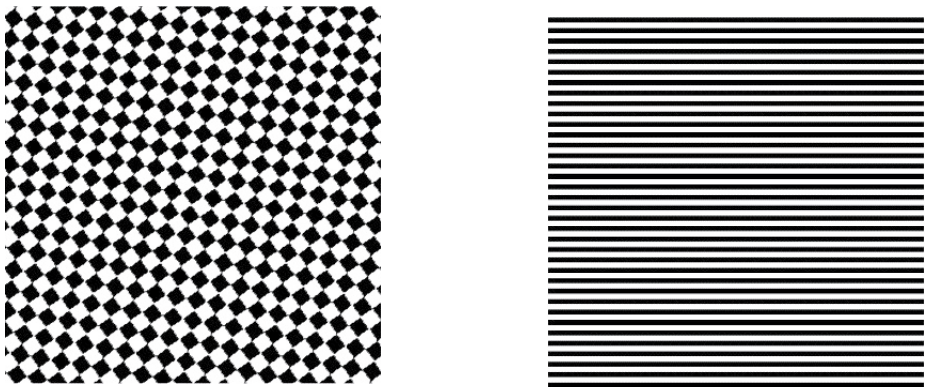

(a) (b)

Figure 19: Non–contoured axial eigenfunctions on the square lattice. (a) square (b) roll.

The case of contoured planforms is more subtle. At a given location $\mathbf{r}$ in V1 we have a sum of two or three sinusoids with different phases and amplitudes (see Tables 3 and 4), which can be written as $a(\mathbf{r},\phi) = A(\mathbf{r})\cos[2\phi - 2\phi_0(\mathbf{r})]$. The phase $\phi_0(\mathbf{r})$ determines the peak of the orientation tuning curve at $\mathbf{r}$ (see figure 14). Hence the

Lattice	Name	Planform Eigenfunction
square	odd square	$u(\phi)\cos x - u\left(\phi - \frac{\pi}{2}\right)\cos y$
	odd roll	$u(\phi)\cos x$
rhombic	odd rhombic	$u(\phi)\cos(\mathbf{k}_1\cdot\mathbf{r}) + u(\phi-\eta)\cos(\mathbf{k}_2\cdot\mathbf{r})$
	odd roll	$u(\phi)\cos(\mathbf{k}_1\cdot\mathbf{r})$
hexagonal	odd hexagon	$u(\phi)\cos(\mathbf{k}_1\cdot\mathbf{r}) + u\left(\phi+\frac{\pi}{3}\right)\cos(\mathbf{k}_2\cdot\mathbf{r}) + u\left(\phi-\frac{\pi}{3}\right)\cos(\mathbf{k}_3\cdot\mathbf{r})$
	triangle	$u(\phi)\sin(\mathbf{k}_1\cdot\mathbf{r}) + u\left(\phi+\frac{\pi}{3}\right)\sin(\mathbf{k}_2\cdot\mathbf{r}) + u\left(\phi-\frac{\pi}{3}\right)\sin(\mathbf{k}_3\cdot\mathbf{r})$
	patchwork quilt	$u\left(\phi+\frac{\pi}{3}\right)\cos(\mathbf{k}_2\cdot\mathbf{r}) - u\left(\phi-\frac{\pi}{3}\right)\cos(\mathbf{k}_3\cdot\mathbf{r})$
	odd roll	$u(\phi)\cos(\mathbf{k}_1\cdot\mathbf{r})$

Table 4: Odd planforms with $u(-\phi) = -u(\phi)$.

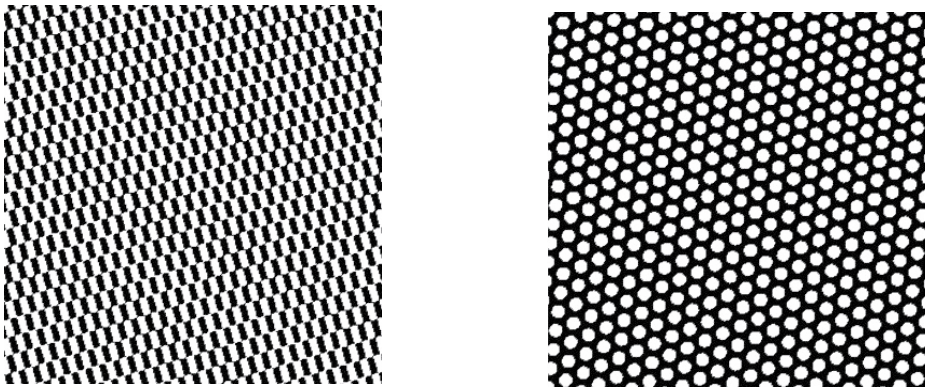

(a) (b)

Figure 20: Non–contoured axial eigenfunctions on rhombic and hexagonal lattices. (a) rhombic (b) hexagonal.

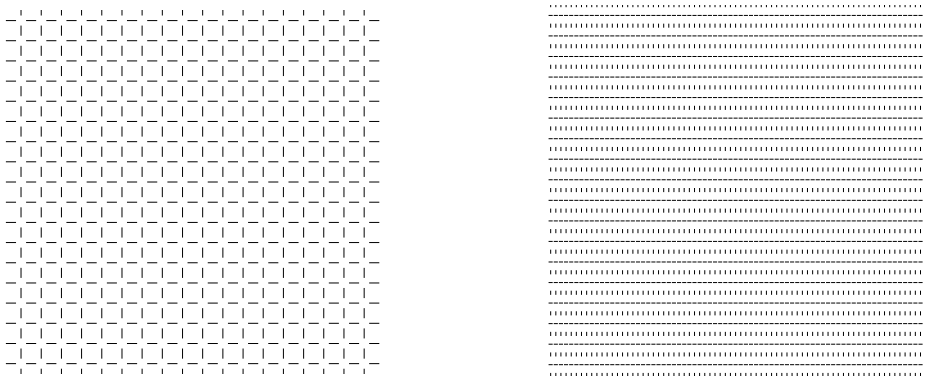

Figure 21: Contours of even axial eigenfunctions on the square lattice. (a) square (b) roll.

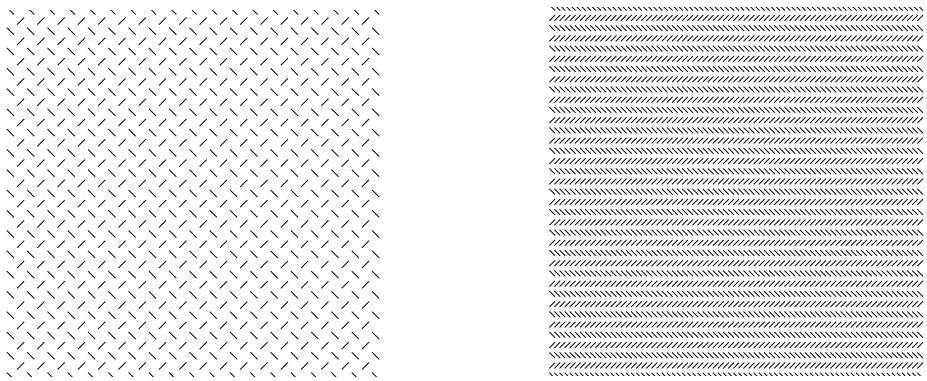

Figure 22: Contours of odd axial eigenfunctions on the square lattice. (a) square (b) roll.

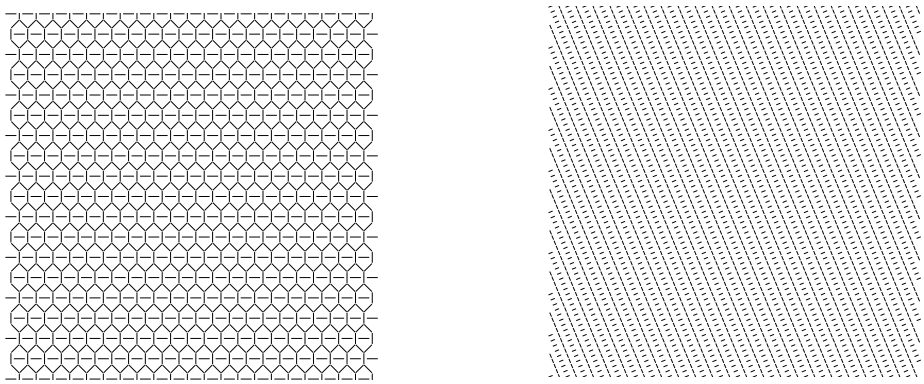

(a) (b)

Figure 23: Contours of even axial eigenfunctions on the rhombic lattice. (a) rhombic (b) roll.

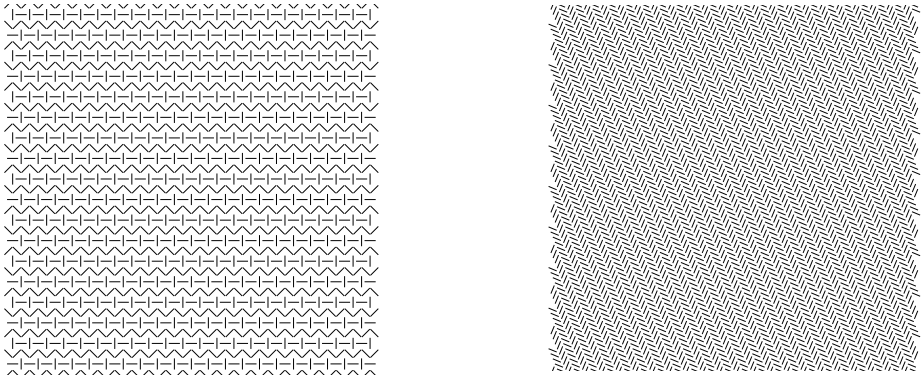

(a) (b)

Figure 24: Contours of odd axial eigenfunctions on the rhombic lattice. (a) rhombic (b) roll.

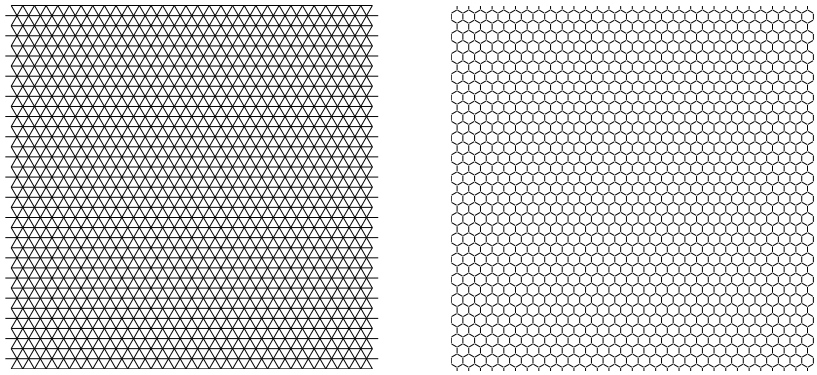

Figure 25: Contours of even axial eigenfunctions on the hexagonal lattice. (a) π–hexagonal (b) 0–hexagonal.

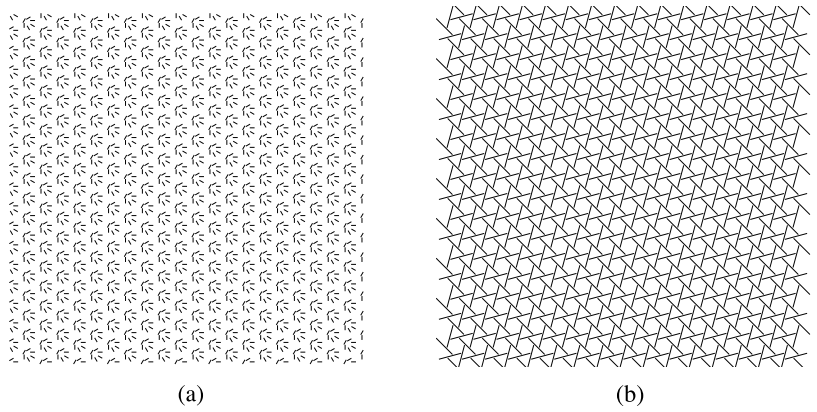

Figure 26: Contours of odd axial eigenfunctions on the hexagonal lattice. (a) triangular (b) 0–hexagonal.

contoured solutions generally consist of iso–orientation regions or patches over which $\phi_0(\mathbf{r})$ is constant but the amplitude $A(\mathbf{r})$ varies. As in the non–contoured case these patches are either square, triangular, or rhombic in shape. However, we now represent each patch to be represented by a locally oriented contour centered at the point of maximal amplitude $A(\mathbf{r}_{max})$ within the patch. The resulting odd and even contoured patterns are shown in figures 21 and 22 for the square latttice, in figures 23 and 24 for the rhombic latttice and in figures 25 and 26 for the hexagonal lattice. Note that our particular interpretation of contoured planforms breaks down in the case of an odd triangle on a hexagonal lattice: the latter comprises hexagonal patches in which all orientations are present with equal magnitudes. In this case we draw a 'star' shape indicating the presence of multiple orientations at a given point, see figure 26(b).

5 From cortical patterns to visual hallucinations

In §4 we derived the generic planforms that bifurcate from the homogeneous state and interpreted them in terms of cortical activity patterns. In order to compute what the various planforms look like in visual field coordinates, we need to apply an inverse retino–cortical map. In the case of non–contoured patterns this can be carried out directly using the (single) retino–cortical map introduced in §1.2. On the other hand, for contoured planforms it is necessary to specify how to map local contours in the visual field as well as position—this is achieved by considering a so called double retino–cortical map. Another important feature of the mapping between V1 and the visual field is that the periodicity of the angular retinal coordinate θ_R implies that the y–coordinate in V1 satisfies cylindrical periodic boundary conditions (see figure 5). This boundary condition should be commensurate with the square, rhombic or hexagonal lattice associated with the doubly periodic planforms.

5.1 The double retino–cortical map

An important consequence of the introduction of orientation as a cortical label is that the retino–cortical map described earlier needs to be extended to cover the mapping

of local contours in the visual field—in effect to treat them as a vector field. Let ϕ_R be the orientation of such a local contour, and ϕ its image in V1. What is the appropriate map from ϕ_R to ϕ that must be added to the map $z_R \to z$ described earlier? We note that a line in V1 of constant slope $\tan\phi$ is a level curve of the equation

$$f(x,y) = y\cos\phi - x\sin\phi$$

where (x,y) are Cartesian coordinates in V1. Such a line has a constant tangent vector

$$\mathbf{v} = \cos\phi\frac{\partial}{\partial x} + \sin\phi\frac{\partial}{\partial y}.$$

The pre–image of such a line in the visual field, assuming the retino–cortical map generated by the complex logarithm is obtained by changing from cortical to retinal coordinates via the complex exponential, is:

$$f(x,y) \to \tilde{f}(r_R,\theta_R) = \theta_R\cos\phi - \log r_R\sin\phi$$

the level curves of which are the logarithmic spirals

$$r_R(\theta_R) = A\,\exp(\cot(\phi)\theta_R).$$

It is easy to show that the tangent vector corresponding to such a curve takes the form

$$\tilde{\mathbf{v}} = r_R\cos(\phi+\theta_R)\frac{\partial}{\partial x_R} + r_R\sin(\phi+\theta_R)\frac{\partial}{\partial y_R}.$$

Thus the retinal vector field induced by a constant vector field in V1 twists with the retinal angle θ_R and stretches with the retinal radius r_R. It follows that if ϕ_R is the orientation of a line in the visual field, then:

$$\phi = \phi_R - \theta_R, \tag{5.1}$$

i.e. local orientation in V1 is relative to the angular coordinate of visual field position. The geometry of the above setup is shown in figure 27.

The resulting double map $\{z_R,\phi_R\} \to \{z,\phi\}$ has very interesting properties. As previously noted, the map $z_R \to z$ takes circles, rays, and logarithmic spirals into

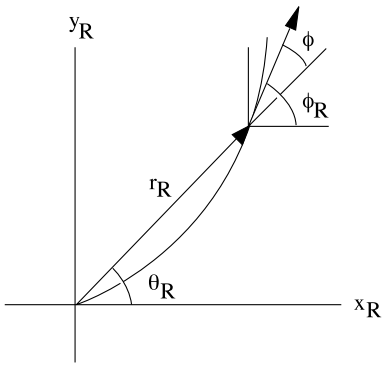

Figure 27: The geometry of orientation tuning.

vertical, horizontal and oblique lines, respectively. What about the extended map? Because the tangent to a circle at a given point is perpendicular to the radius at that point, for circles, $\phi_R = \theta_R + \pi/2$, so that $\phi = \pi/2$. Similarly, for rays, $\phi_R = \theta_R$, so $\phi = 0$. For logarithmic spirals we can write either $\theta_R = a \ln r_R$ or $r_R = \exp[b\theta_R]$. In retinal coordinates we find the somewhat cumbersome formula

$$\tan \phi_R = \frac{br_R \sin \theta_R + e^{b\theta_R} \cos \theta_R}{br_R \cos \theta_R - e^{b\theta_R} \sin \theta_R}.$$

However this can be rewritten as $\tan(\phi_R - \theta_R) = a$, so that in V1 coordinates, $\tan \phi = a$. Thus we see that the local orientations of circles, rays and logarithmic spirals, measured in relative terms, all lie along the cortical images of such forms. Figure 28 shows the details.

5.2 Planforms in the visual field

In order to generate a visual field pattern we split our model V1 domain $\mathcal{M}$ into two pieces each running 72 mm along the x direction and 48 mm along the y direction, representing the right and left hemifields in the visual field (see figure 5). Since the y coordinate corresponds to a change from $-\pi/2$ to $\pi/2$ in 48 mm which meets up again smoothly with the representation in the opposite hemifield, we must only choose scalings and rotations of our planforms that satisfy cylindrical periodic boundary

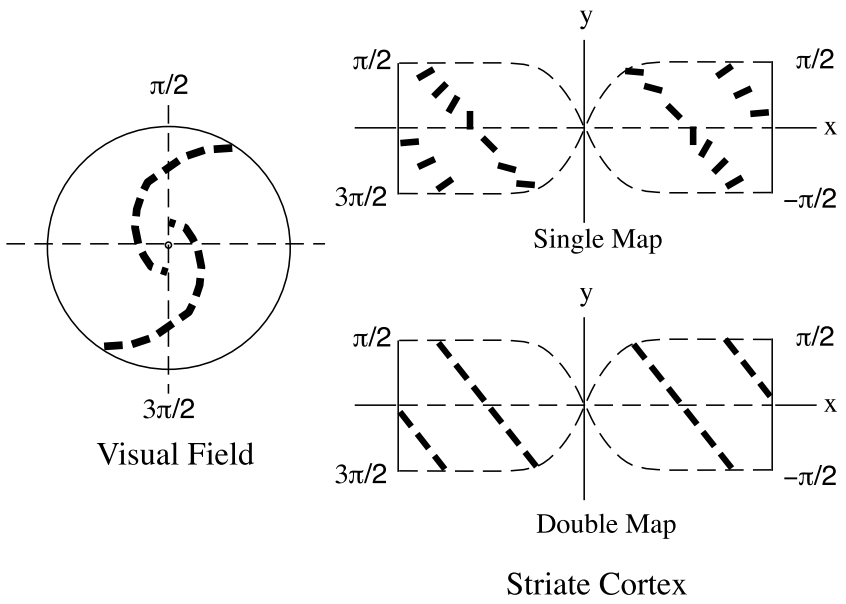

Figure 28: Action of the single and double maps on logarithmic spirals. Dashed lines show the local tangents to a logarithmic spiral contour in the visual field, and the resulting image in V1. Since circle and ray contours in the visual field are just special cases of logarithmic spirals, the same result holds also for such contours.

conditions in the y direction. In the x direction, corresponding to the logarithm of radial eccentricity, we neglect the region immediately around the fovea as well as the far edge of the periphery, so we have no constraint on the patterns in this direction.

Recall that each V1 planform is doubly periodic with respect to a spatial lattice generated by two lattice vectors $\boldsymbol{\ell}_1, \boldsymbol{\ell}_2$. The cylindrical periodicity is thus equivalent to requiring that there be an integral combination of lattice vectors that spans $Y = 96$ mm in the y direction with no change in the x direction:

$$\begin{pmatrix} 0 \\ 96 \end{pmatrix} = 2\pi m_1 \boldsymbol{\ell}_1 + 2\pi m_2 \boldsymbol{\ell}_2 \tag{5.2}$$

If the acute angle of the lattice η' is specified, then the wavevectors $\mathbf{k}_i$ are determined

by the requirement

$$\mathbf{k}_i \cdot \boldsymbol{\ell}_j = \begin{cases} 1, i = j \\ 0, i \neq j. \end{cases} \tag{5.3}$$

The integral combination requirement limits which wavelengths are permitted for planforms in the cortex. The length scale for a planform is given by the length of the lattice vectors $|\boldsymbol{\ell}_1| = |\boldsymbol{\ell}_2| := |\boldsymbol{\ell}|$:

$$|\boldsymbol{\ell}| = \frac{96}{\sqrt{m_1^2 + 2m_1 m_2 \cos(\eta') + m_2^2}} \tag{5.4}$$

The commonly reported hallucination patterns usually have thirty to forty repetitions of the pattern around a circumference of the visual field, corresponding to length scales ranging from $2.4 - 3.2$ mm. Therefore, we would expect the critical wavelength $2\pi/q_c$ for bifurcations to be in this range. [see § 3.3] Note that when we rotate the planform to match the cylindrical boundary conditions we rotate $\mathbf{k}_1$ and hence the maximal amplitude orientations $\phi_0(\mathbf{r})$ by

$$\cos^{-1}[\frac{m_2|\boldsymbol{\ell}|}{Y}\sin(\eta')] + \eta' - \pi/2.$$

The resulting non–contoured planforms in the visual field obtained by applying the inverse single retino–cortical map to the corresponding V1 planforms are shown in figures 29 and 30.

Similarly the odd and even contoured planforms obtained by applying the double retino–cortical map are shown in figures 31 and 32 for the square latttice, in figures 33 and 34 for the rhombic latttice, and in figures 35 and 36 for the hexagonal lattice.

One of the striking features of the resulting (contoured) visual planforms is that only the even planforms appear to be contour completing and it is these that recover the remaining form constants missing from the original Ermentrout–Cowan model. The reader should compare, for example, the pressure phosphenes shown in figure 1 with figure 35(a), and the cobweb of figure 4 with figure 31(a).

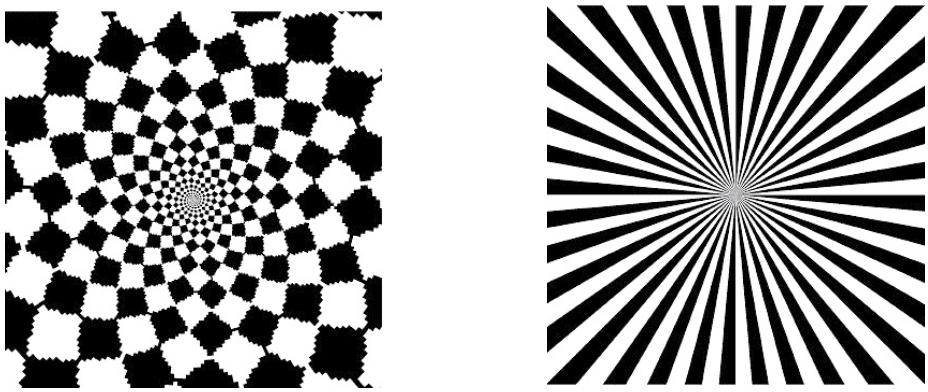

(a) (b)

Figure 29: Action of the single inverse retino–cortical map on non–contoured square planforms. (a) square (b) roll.

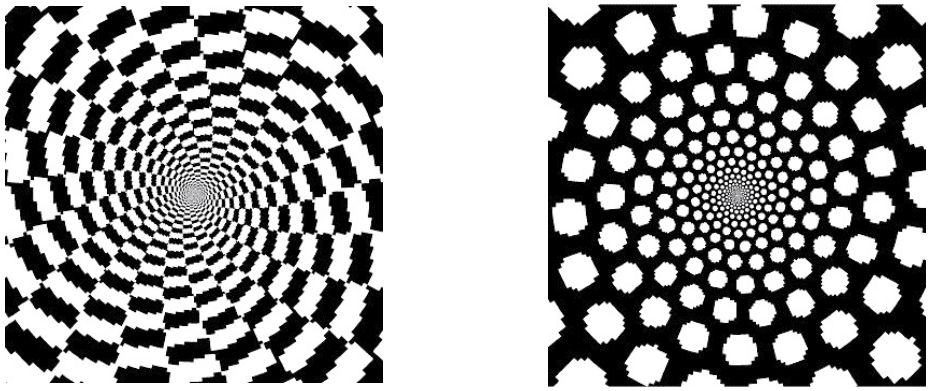

(a) (b)

Figure 30: Action of the single inverse retino–cortical map on non–contoured rhombic and hexagonal planforms. (a) rhombic (b) hexagonal.

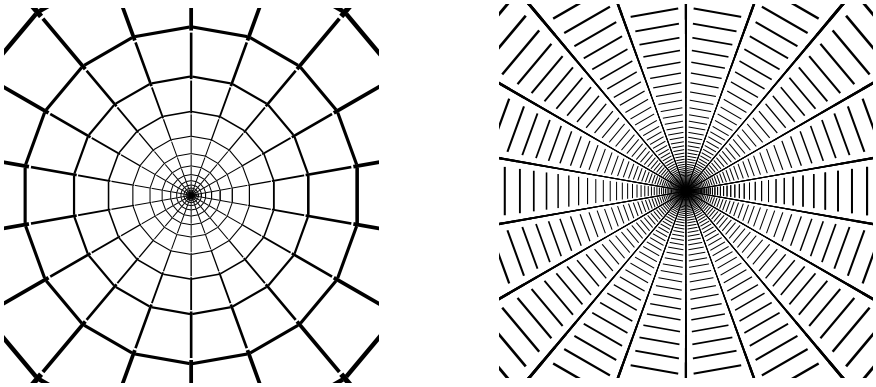

Figure 31: Action of the double inverse retino–cortical map on even square planforms. (a) square (b) roll.

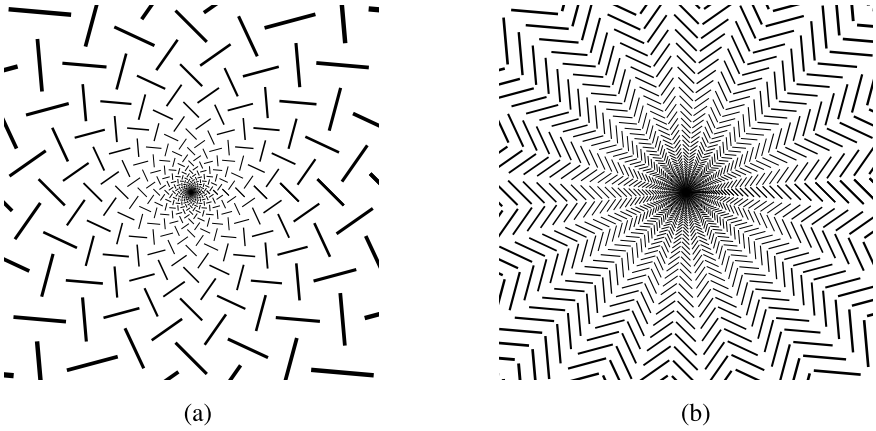

Figure 32: Action of the double inverse retino–cortical map on odd square planforms. (a) square (b) roll.

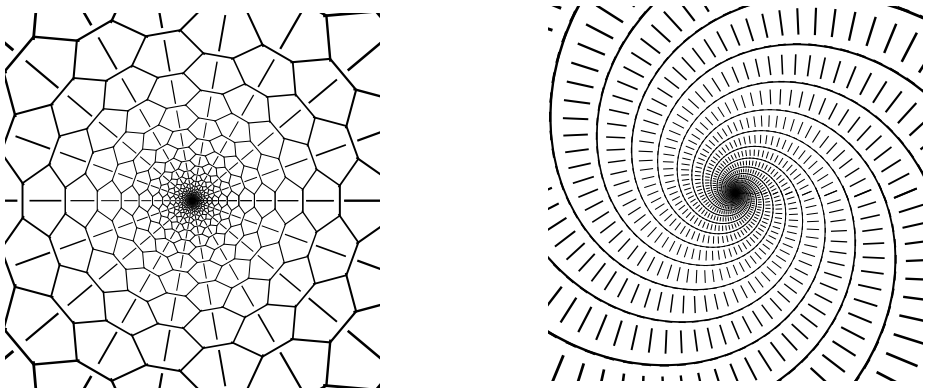

(a) (b)

Figure 33: Action of the double inverse retino–cortical map on even rhombic planforms. (a) rhombic (b) roll.

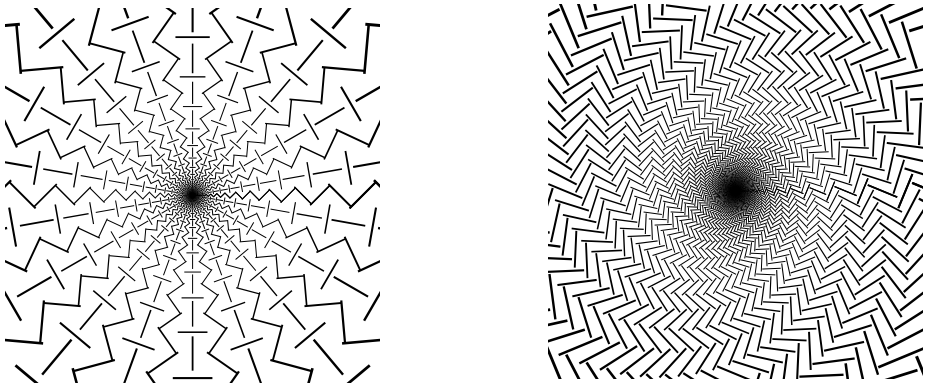

(a) (b)

Figure 34: Action of the double inverse retino–cortical map on odd rhombic planforms. (a) rhombic (b) roll.

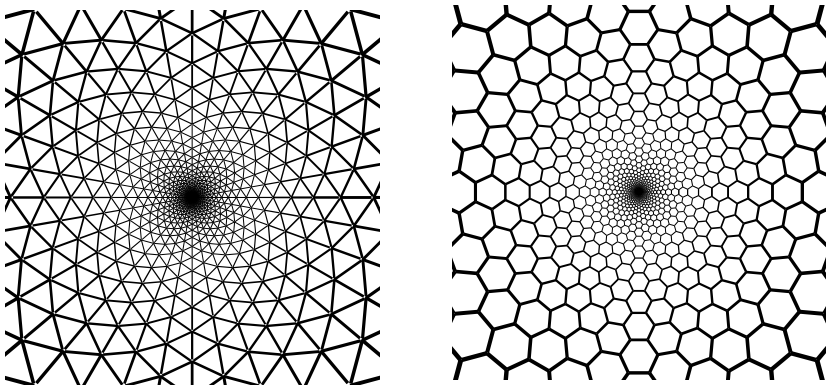

(a) (b)

Figure 35: Action of the double inverse retino–cortical map on even hexagonal planforms. (a) π–hexagonal (b) 0–hexagonal.

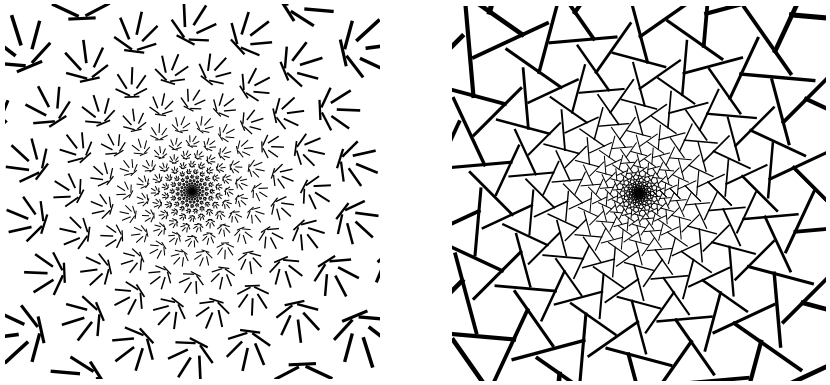

(a) (b)

Figure 36: Action of the double inverse retino–cortical map on odd hexagonal planforms. (a) triangular (b) 0–hexagonal.

6 The Selection and stability of patterns

It remains to determine which of the various planforms we have presented above are actually stable in our model, for biologically relevant parameter sets. So far we have used a mixture of perturbation theory and symmetry to construct the linear eigenmodes (3.17) that are candidate planforms for pattern forming instabilities. To determine which of these modes are stabilized by the nonlinearities of the system we use techniques such as Liapunov–Schmidt reduction and Poincaré–Lindstedt perturbation theory to reduce the dynamics to a set of nonlinear equations for the amplitudes c_i appearing in equation (3.17) (Walgraef, 1997). These amplitude equations, which effectively describe the dynamics on a finite–dimensional center manifold, then determine the selection and stability of patterns (at least sufficiently close to the bifurcation point). The symmetries of the system severely restrict the allowed forms (Golubitsky *et al.*, 1988). On the other hand, the coefficients in this form are inherently model–dependent and have to be calculated explicitly.

In this section we determine the amplitude equation for our cortical model up to cubic order and use this to investigate the selection and stability of both odd patterns satisfying $u(-\phi) = -u(\phi)$ and even patterns satisfying $u(-\phi) = u(\phi)$. A more complete discussion of stability and selection based on symmetric bifurcation theory, which takes into account the possible effects of higher–order contributions to the amplitude equation, will be presented elsewhere (Bressloff *et al.*, 2000b).

6.1 The Cubic amplitude equation

Assume that sufficiently close to the bifurcation point at which the homogeneous state $a(\mathbf{r}, \phi) = 0$ becomes marginally stable, the excited modes grow slowly at a rate $\mathcal{O}(\epsilon^2)$ where $\epsilon^2 = \mu - \mu_c$. One can then use the method of multiple–scales to perform a Poincaré–Lindstedt perturbation expansion in ϵ. First Taylor expand the nonlinear function $\sigma[a]$ appearing in equation (2.11),

$$\sigma[a] = \sigma_1 a + \sigma_2 a^2 + \sigma_3 a^3 + \dots$$

where $\sigma_1 = \sigma'[0]$, $\sigma_2 = \sigma''[0]/2$, $\sigma_3 = \sigma'''[0]/3!$ etc. Then perform a perturbation expansion of equation (2.11) with respect to ϵ by writing

$$a = \epsilon a_1 + \epsilon^2 a_2 + \dots$$

and introducing a slow time–scale $\tau = \epsilon^2 t$. Collecting terms with equal powers of ϵ then generates a hierarchy of equations as shown in appendix A.3. The $\mathcal{O}(\epsilon)$ equation is equivalent to the eigenvalue equation (3.10) with $\lambda = 0$, $\mu = \mu_c$ and $|\mathbf{k}| = q_c$ so that

$$a_1(\mathbf{r}, \phi, t) = \sum_{j=1}^{N} c_j(t) \mathrm{e}^{i\mathbf{k}_j \cdot \mathbf{r}} u(\phi - \varphi_j) + c.c. \tag{6.1}$$

with $\mathbf{k}_j = q_c(\cos\varphi_j, \sin\varphi_j)$. Requiring that the $\mathcal{O}(\epsilon^2)$ and $\mathcal{O}(\epsilon^3)$ equations in the hierarchy be self–consistent then leads to a solvability condition which in turn generates evolution equations for the amplitudes $c_j(t)$ (see appendix A.3).

Square or rhombic lattice First, consider planforms (6.1) corresponding to a bimodal structure of the square or rhombic type ($N = 2$). That is, take $\mathbf{k}_1 = q_c(1, 0)$ and $\mathbf{k}_2 = q_c(\cos(\theta), \sin(\theta))$, with $\theta = \pi/2$ for the square lattice and $0 < \theta < \pi/2$, $\theta \neq \pi/3$ for a rhombic lattice. The amplitudes evolve according to a pair of equations of the form

$$\begin{aligned} \frac{dc_1}{dt} &= c_1 \left[\Lambda - \gamma_0 |c_1|^2 - 2\gamma_\theta |c_2|^2\right] \\ \frac{dc_2}{dt} &= c_2 \left[\Lambda - \gamma_0 |c_2|^2 - 2\gamma_\theta |c_1|^2\right] \end{aligned} \tag{6.2}$$

where $\Lambda = \mu - \mu_c$ measures the deviation from the critical point, and

$$\gamma_\varphi = \frac{3\alpha|\sigma_3|}{\sigma_1} \Gamma^{(3)}(\varphi) \tag{6.3}$$

for all $0 \leq \varphi < \pi$ with

$$\Gamma^{(3)}(\varphi) = \int_0^\pi u(\phi - \varphi)^2 u(\phi)^2 \frac{d\phi}{\pi} \tag{6.4}$$

Hexagonal lattice Next consider planforms on a hexagonal lattice with $N = 3$, $\varphi_1 = 0$, $\varphi_2 = 2\pi/3$, $\varphi_3 = -2\pi/3$. The cubic amplitude equations take the form

$$\frac{dc_j}{dt} = c_j \left[\Lambda - \gamma_0|c_j|^2 - 2\gamma_{2\pi/3}(|c_{j+1}|^2 + |c_{j-1}|^2)\right] + \eta \overline{c}_{j-1}\overline{c}_{j+1} \tag{6.5}$$

where $j = 1, 2, 3 \mod 3$, $\gamma_{2\pi/3}$ is given by (6.4) for $\varphi = 2\pi/3$, and

$$\eta = \frac{\alpha\sigma_2}{\sigma_1\sqrt{\sigma_1 W_1}}\Gamma^{(2)} \tag{6.6}$$

with

$$\Gamma^{(2)} = \int_0^\pi u(\phi)u(\phi - 2\pi/3)u(\phi + 2\pi/3)\frac{d\phi}{\pi} \tag{6.7}$$

In deriving equation (6.5) we have assumed that the neurons are operating close to threshold such that $\sigma_2 = \mathcal{O}(\epsilon)$.

The basic structure of equations (6.2) and (6.5) is universal in the sense that it only depends on the underlying symmetries of the system and on the type of bifurcation that it is undergoing. On the other hand, the actual values of the coefficients γ_φ and η are model–dependent and have to be calculated explicitly. Moreover, these coefficients are different for odd and even patterns due to the fact that they have distinct eigenfunctions $u(\phi)$. Note also that because of symmetry the quadratic term in equation (6.5) must vanish identically in the case of odd patterns.

Even contoured planforms Substituting the perturbation expansion of the eigenfunction (3.14) for even contoured planforms into equations (6.7) and (6.4) gives

$$\Gamma^{(2)} = \frac{3}{4}\beta[u_2^+(q_c) - u_0^+(q_c)] + \mathcal{O}(\beta^2) \tag{6.8}$$

$$\Gamma^{(3)}(\theta) = \frac{1}{8}\left[2 + \cos(4\theta) + 4\beta u_3^+(q_c)\cos(4\theta) + \mathcal{O}(\beta^2)\right] \tag{6.9}$$

with the coefficients u_n^+ defined by equation (3.16).

Odd contoured planforms Substituting the perturbation expansion of the eigenfunction (3.15) for odd contoured planforms into equations (6.7) and (6.4) gives

$$\Gamma^{(2)} = 0 \tag{6.10}$$

$$\Gamma^{(3)}(\theta) = \frac{1}{8}\left[2 + \cos(4\theta) - 4\beta u_3^-(q_c)\cos(4\theta) + \mathcal{O}(\beta^2)\right] \tag{6.11}$$

with the coefficients u_n^- defined by equation (3.16). Note that the quadratic term in equation (6.5) vanishes identically in the case of odd patterns.

Even non–contoured planforms Substituting the perturbation expansion of the eigenfunction (3.24) for even non–contoured planforms into equations (6.7) and (6.4) gives

$$\Gamma^{(2)} = 1 + \frac{3}{2}\beta^2 \sum_{m>0} \left[u_m^0(q_c)\right]^2 \cos(2m\pi/3) + \mathcal{O}(\beta^3) \tag{6.12}$$

$$\Gamma^{(3)}(\theta) = 1 + \beta^2 \sum_{m>0} \left[u_m^0(q_c)\right]^2 [1 + 2\cos(2m\theta)] + \mathcal{O}(\beta^3) \tag{6.13}$$

with the coefficients u_n^0 defined by equation (3.25).

6.2 Even and odd patterns on square or rhombic lattices

We now use equation (6.2) to investigate the selection and stability of odd or even patterns on square or rhombic lattices. Assuming that $\gamma_\theta > 0$ and $\Lambda > 0$, three types of steady state are possible.

1. The homogeneous state: $c_1 = c_2 = 0$.
2. Rolls: $c_1 = \sqrt{\Lambda/\gamma_0}\mathrm{e}^{i\psi_1}, c_2 = 0$ or $c_1 = 0, c_2 = \sqrt{\Lambda/\gamma_0}\mathrm{e}^{i\psi_2}$.
3. Squares or rhombics: $c_1 = \sqrt{\Lambda/[\gamma_0 + 2\gamma_\theta]}\mathrm{e}^{i\psi_1}, c_2 = \sqrt{\Lambda/[\gamma_0 + 2\gamma_\theta]}\mathrm{e}^{i\psi_2}$.

for arbitrary phases ψ_1, ψ_2. The non–trivial solutions correspond to the axial planforms listed in Tables 3 and 4. A standard linear stability analysis shows that if $2\gamma_\theta > \gamma_0$ then rolls are stable whereas the square or rhombic patterns are unstable. The opposite holds if $2\gamma_\theta < \gamma_0$. These stability properties persist when higher order terms in the amplitude equation are included (Bressloff *et al.*, 2000b).

Using equations (6.3), (6.9), (6.11) and (6.13) with $3\alpha|\sigma_3|/\sigma_1 = 1$, we deduce that

$$2\gamma_\theta = \gamma_0 + 1 + \mathcal{O}(\beta)$$

for non–contoured patterns, and

$$2\gamma_\theta = \gamma_0 + [1 + 2\cos(4\theta)]/8 + \mathcal{O}(\beta)$$

for (odd or even) contoured patterns. Hence, in the case of a square or rhombic lattice we have the following results concerning patterns bifurcating from the homogeneous state close to the point of marginal stability (in the limit of weak lateral interactions):

> For non–contoured patterns on a square or rhombic lattice there exist stable rolls and unstable squares.
>
> For (even or odd) contoured patterns on a square lattice there exist stable rolls and unstable squares. In the case of a rhombic lattice of angle $\theta \neq \pi/2$, rolls are stable if $\cos(4\theta) > -1/2$ whereas θ–rhombics are stable if $\cos(4\theta) < -1/2$, that is, if $\pi/6 < \theta < \pi/3$.

It should be noted that this result differs from that obtained by Ermentrout & Cowan (1979) in which stable squares were shown to occur for certain parameter ranges [see also Ermentrout (1991)]. We attribute this difference to the anisotropy of the lateral connections incorporated into the current model and the consequent shift-twist symmetry of the Euclidean group action. The effects of this anisotropy persist even in the limit of weak lateral connections, and preclude the existence of stable square patterns.

6.3 Even patterns on a hexagonal lattice

Next we use equations (6.5) and (6.6) to analyze the stability of even planforms on a hexagonal lattice. On decomposing $c_i = C_i e^{i\psi_i}$, it is a simple matter to show that two of the phases ψ_i are arbitrary while the sum $\psi = \sum_{i=1}^{3} \psi_i$ and the real amplitudes C_i evolve according to the equations

$$\frac{dC_i}{dt} = \Lambda C_i + \eta C_{i+1} C_{i-1} \cos\psi - \gamma_0 C_i^3 - 2\gamma_{2\pi/3}(C_{i+1}^2 + C_{i-1}^2) C_i \tag{6.14}$$

and

$$\frac{d\psi}{dt} = -\eta \sum_{i=1}^{3} \frac{C_{i+1} C_{i-1}}{C_i} \sin\psi \tag{6.15}$$

with $i, j = 1, 2, 3 \mod 3$. It immediately follows from equation (6.15) that the stable steady state solution will have a phase $\psi = 0$ if $\eta > 0$ and a phase $\psi = \pi$ if $\eta < 0$.

From equations (6.3) (6.9) and (6.13) with $3\alpha|\sigma_3|/\sigma_1 = 1$ we see that

$$2\gamma_{2\pi/3} = \gamma_0 + 1 + \mathcal{O}(\beta^2)$$

for even non–contoured patterns, and

$$2\gamma_{2\pi/3} = \gamma_0 + \beta u_3^-(q_c) + \mathcal{O}(\beta^2)$$

for even contoured patterns. In the parameter regime where the marginally stable modes are even contoured planforms (such as in figure 17) we find that $u_3^+(q_c) > 0$. This is illustrated in figure 37.

Therefore, $2\gamma_{2\pi/3} > \gamma_0$ for both the contoured and non–contoured cases. Standard analysis then shows that (to cubic order) there exists a stable hexagonal pattern $C_i = C$ for $i = 1, 2, 3$ with amplitude (Busse, 1962)

$$C = \frac{1}{2[\gamma_0 + 4\gamma_{2\pi/3}]} \left[|\eta| + \sqrt{\eta^2 + 4[\gamma_0 + 4\gamma_{2\pi/3}]\Lambda} \right] \tag{6.16}$$

over the parameter range

$$\frac{-\eta^2}{4[\gamma_0 + 4\gamma_{2\pi/3}]} < \Lambda < \frac{2\eta^2[\gamma_0 + \gamma_{2\pi/3}]}{[\gamma_0 - 2\gamma_{2\pi/3}]^2}$$

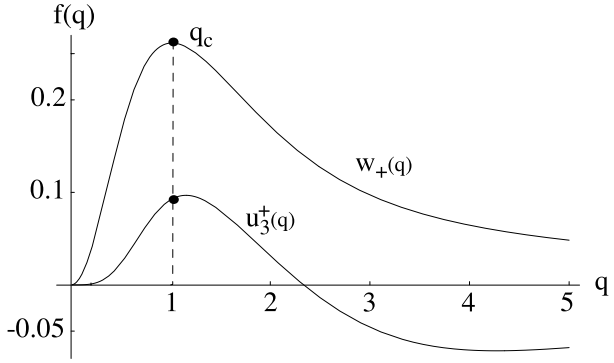

Figure 37: Plot of the even eigenfunction coefficient $u_3^+(q)$ of equation (3.16) as a function of wavenumber q. Also plotted is the $\mathcal{O}(\beta)$ contribution to the even eigenvalue expansion, equation (3.13), $w_+(q) = \hat{W}_0(q) + \hat{W}_2(q)$. The peak of $w_+(q)$ determines the critical wavenumber q_c (to first order in β). Same parameter values as figure 17.

The maxima of the resulting hexagonal pattern are located on an equilateral triangular lattice for $\eta > 0$ (0–hexagons) whereas the maxima are located on an equilateral hexagonal lattice for $\eta < 0$ (π–hexagons). Both classes of hexagonal planform have the same $\mathbf{D}_6$ axial subgroup (up to conjugacy), see Table 7 in appendix A.2. One can also establish that rolls are unstable versus hexagonal structures in the range

$$0 < \Lambda < \frac{\eta^2}{[\gamma_0 - 2\gamma_{2\pi/3}]^2} \tag{6.17}$$

Hence, in the case of a hexagonal lattice we have the following result concerning the even patterns bifurcating from the homogeneous state close to the point of marginal stability (in the limit of weak lateral interactions):

> For even (contoured or non–contoured) patterns on a hexagonal lattice, stable hexagonal patterns are the first to appear (subcritically) beyond the bifurcation point. Subsequently the stable hexagonal branch exchanges stability with an unstable branch of roll patterns as shown in figure 38.

Techniques from symmetric bifurcation theory can be used to investigate the effects of higher order terms in the amplitude equation (Buzano & Golubitsky, 1983): in

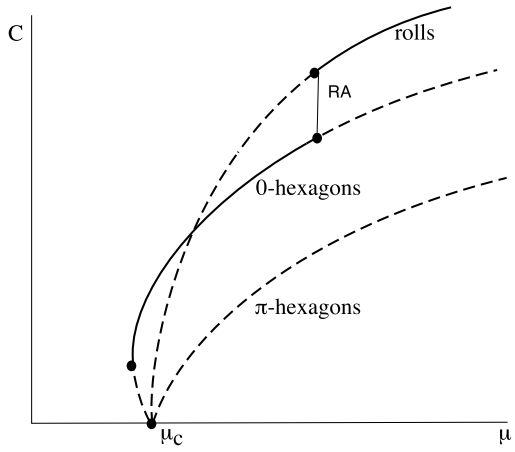

Figure 38: Bifurcation diagram showing the variation of the amplitude C with the parameter μ for even hexagonal and roll patterns with $\eta > 0$. Solid and dashed curves indicate stable and unstable solutions respectively. Also shown is a secondary branch of rectangular patterns RA. Higher–order terms in the amplitude equation are needed to determine its stability.

the case of even planforms the results are identical to those obtained in the analysis of Bénard convection in the absence of midplane symmetry. For example, one finds that the exchange of stability between the hexagons and rolls is due to a secondary bifurcation that generates rectangular patterns.

6.4 Odd patterns on a hexagonal lattice

Recall that in the case of odd patterns, the quadratic term in equation (6.5) vanishes identically. The homogeneous state now destabilizes via a (supercritical) pitchfork bifurcation to the four axial planforms listed in Tables 3 and 4. In this particular case it is necessary to include higher–order (quartic and quintic terms) in the amplitude equation to completely specify the stability of these various solutions, and to identify possible secondary bifurcations. Unfortunately one cannot carry over previous results obtained from the study of the Bénard convection problem with midplane symmetry,

even though the corresponding amplitude equation is identical in structure at cubic order (Golubitsky, Swift, & Knobloch, 1984): higher–order contributions to the amplitude equation will differ in the two problems due to the radically different actions of the Euclidean group and the resulting differences in the associated axial subgroups[1]. The effects of such contributions on the bifurcation structure of odd (and even) cortical patterns will be studied in detail elsewhere (Bressloff *et al.*, 2000b). Here, we simply describe the more limited stability results that can be deduced at cubic order.

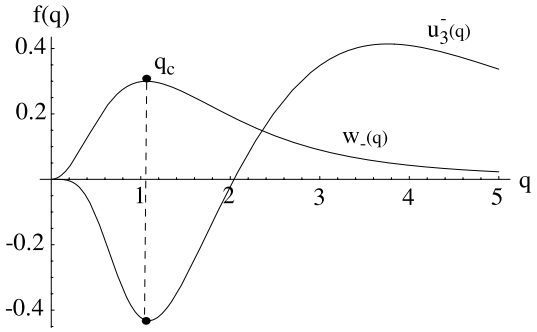

Figure 39: Plot of the odd eigenfunction coefficient $u_3^-(q)$ of equation (3.16) as a function of wavenumber q. Also plotted is the $\mathcal{O}(\beta)$ contribution to the odd eigenvalue expansion, equation (3.13), $w_-(q) = \hat{W}_0(q) - \hat{W}_2(q)$. The peak of $w_-(q)$ determines the critical wavenumber q_c (to first order in β). Same parameter values as figure 16.

A basic question concerns which of the four odd planforms on a hexagonal lattice (hexagons, triangles, patchwork quilts and rolls) are stable. It turns out that if $2\gamma_{2\pi/3} > \gamma_0$ then rolls are stable, whereas if $2\gamma_{2\pi/3} < \gamma_0$ then either hexagons or triangles are stable (depending upon higher–order terms). Equations (6.4) and (6.11) with $3\alpha|\sigma_3|/\sigma_1 = 1$ imply that

$$2\gamma_{2\pi/3} = \gamma_0 + \beta u_3^-(q_c) + \mathcal{O}(\beta^2) \tag{6.18}$$

In the parameter regime where the marginally stable modes are odd contoured planforms (such as in figure 16) we find that $u_3^-(q_c) < 0$, and thus $2\gamma_{2\pi/3} < \gamma_0$. This is

[1]Interestingly, there does exist an example from fluid dynamics where the modified Euclidean group action (2.9) arises (Bosch Vivancos *et al.*, 1995)

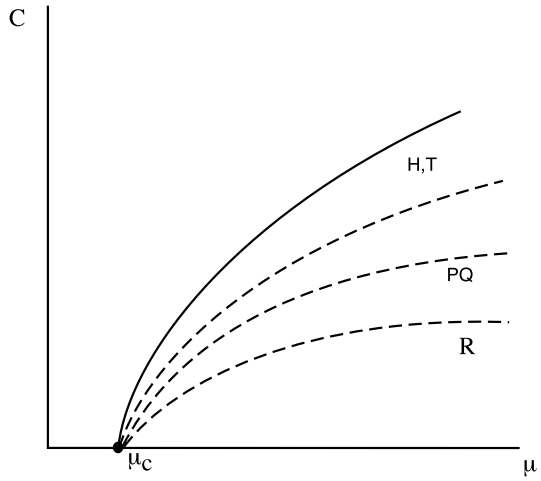

Figure 40: Bifurcation diagram showing the variation of the amplitude C with the parameter μ for odd patterns on a hexagonal lattice. Solid and dashed curves indicate stable and unstable solutions respectively. Either hexagons (H) or triangles (T) are stable (depending on higher–order terms in the amplitude equation) whereas patchwork quilts (PQ) and rolls (R) are unstable. Secondary bifurcations (not shown) may arise from higher–order terms (Bressloff *et al.*, 2000b).

illustrated in figure 39. Hence, in the case of a hexagonal lattice we have the following result concerning the odd patterns bifurcating from the homogeneous state close to the point of marginal stability (in the limit of weak lateral interactions):

> For odd (contoured) patterns on a hexagonal lattice there exist four primary bifurcation branches corresponding to hexagons, triangles, patchwork quilts and rolls. Either the hexagons or the triangles are stable (depending on higher–order terms through a secondary bifurcation) and all other branches are unstable. This is illustrated in figure 40.

7 Discussion

This paper describes a new model of the spontaneous generation of patterns in V1 (seen as geometric hallucinations). Whereas the earlier work of Ermentrout & Cowan started with a general neural network and sought the minimal restrictions necessary to produce hallucination patterns, the current model incorporates data gathered over the last two decades to show that common hallucinatory images can be generated by a biologically plausible architecture in which the connections between iso–orientation patches in V1 are locally isotropic, but non–locally anisotropic. As we, and Ermentrout & Cowan before us show, the Euclidean symmetry of such an architecture, that is, the symmetry with respect to rigid motions in the plane, plays a key role in determining which patterns of activation of the iso–orientation patches appear when the homogeneous state becomes unstable, presumed to occur, for example, shortly after the action of hallucinogens on those brain stem nuclei that control cortical excitability.

There are, however, two important differences between the current work and that of Ermentrout & Cowan in the way in which the Euclidean group is implemented:

(a) The group action is different and novel, and so the way in which the various subgroups of the Euclidean group are generated is significantly different. In particular, the various planforms corresponding to the subgroups are labeled by orientation preference, as well as by their location in the cortical plane. It follows that the eigenfunctions which generate such planforms are also labeled in such a fashion. This adds an additional complication to the problem of calculating such eigenfunctions and the eigenvalues to which they belong, from the linearized cortical dynamics. Assuming that the non–local lateral or horizontal connections are modulatory and weak relative to the local connections, we show how the methods of Rayleigh–Schrödinger degenerate perturbation theory can be used to compute, to some appropriate level of approximation, the requisite eigenvalues and eigenfunctions, and therefore the planforms. Given such eigenfunctions we then make use of Poincaré–Lindstedt perturbation theory to compute the stability of the various planforms that appear when the homogeneous state becomes unstable.

(b) Since we include orientation preference in the formulation, we have to consider the action of the retino–cortical map on oriented contours or edges. In effect we do this by treating the local tangents to such contours as a vector field. As we discussed, this is carried out by the tangent map associated with the complex logarithm, one consequence of which is that ϕ, the V1 label for orientation preference, is not exactly equal to orientation preference in the visual field, ϕ_R, but differs from it by the angle θ_R, the polar angle of receptive field position. We called the map from visual field coordinates $\{r_R, \theta_R, \phi_R\}$ to V1 coordinates $\{x, y, \phi\}$ a double map. Its possible presence in V1 is subject to experimental verification. If the double map is present, then elements tuned to the same relative angle ϕ should be connected with greater strength than others; if only the single map $\{r_R, \theta_R\} \to \{x, y\}$ obtains, then elements tuned to the same absolute angle ϕ_R should be so connected. If in fact the double map is present, then elements tuned to the same angle ϕ should be connected along lines at that angle in V1. This would support Mitchison & Crick's hypothesis on connectivity in V1 (Mitchison & Crick, 1982) and would be consistent with the observations of Blasdel and Sincich [personal communication] and Bosking *et al.* (1997). In this connection it is of interest that from equation (5.1) it follows that near the vertical meridian (where most of the observations have been made), changes in ϕ approximate closely changes in ϕ_R. However, a prediction of the double map is that such changes should be relatively large and detectable with optical imaging, near the horizontal meridian.

The main advance over the Ermentrout–Cowan work is that all the Klüver form constants can now be obtained as planforms associated with axial subgroups of the Euclidean group in the plane, generated by the new representations we have discovered. There are several aspects of this work which require comment:

(a) The analysis indicates that under certain conditions the planforms are either contoured or else non–contoured, depending on the strength of inhibition between neighboring iso–orientation patches. If such inhibition is weak, individual hypercolumns do not exhibit any tendency to amplify any particular orientation.

In normal circumstances such a preference would have to be supplied by inputs from the LGN. In this case, V1 can be said to operate in the Hubel–Wiesel mode [see § 2.3]. If the horizontal interactions are still effective, then plane waves of cortical activity can emerge, with no label for orientation preference. The resulting planforms are called non–contoured, and correspond to a subset of the Klüver form constants: tunnels and funnels, and spirals. Conversely, if there is strong inhibition between neighboring iso–orientation patches, even weakly biased inputs to a hypercolumn can trigger a sharply tuned response such that, under the combined action of many interacting hypercolumns, plane waves labeled for orientation preference can emerge. The resulting planforms correspond to contoured patterns and to the remaining form constants described by Klüver—honeycombs and checkerboards, and cobwebs. Interestingly, all but the square planforms are stable. But there do exist hallucinatory images that correspond to square planforms. It is possible that these are just transitional forms.

(b) Another conclusion to be drawn from this analysis is that the circuits in V1 which are normally involved in the detection of oriented edges and the formation and processing of contours, are also responsible for the generation of the hallucinatory form constants. Thus, we introduced in § 2.1 a V1 model circuit in which the lateral connectivity is anisotropic and inhibitory. [We noted in § 1.4 that 20% of the (excitatory) lateral connections in layers II and III of V1 end on inhibitory inter–neurons, so the overall action of the lateral connections could become inhibitory, especially at high levels of activity.] As we demonstrated in § 3.3 the mathematical consequences of this is the selection of odd planforms. But these do not form continuous contours [see § 5.2]. This is consistent with the possibility that such connections are involved in the segmentation of visual images (Li, 1999). In order to select even planforms, which are contour forming and correspond to seen form constants, it proved sufficient to allow for deviation away from the visuotopic axis by at least 45^o in the pattern of lateral connections between iso–orientation patches. These results are consistent with observations that suggest that there are two circuits in V1, one dealing with contrast edges,

in which the relevant lateral connections have the anisotropy found by Blasdel and Sincich [personal communication] and Bosking *et al.* (1997), and another that might be involved with the processing of textures, surfaces and color contrast, and which has a much more isotropic lateral connectivity (Livingstone & Hubel, 1984). One can interpret the less anisotropic pattern needed to generate even planforms as a composite of the two circuits.

There are also two other intriguing possible scenarios which are consistent with our analysis. The first was referred to in § 3.4. In case V1 is operating in the Hubel–Wiesel mode, with no intrinsic tuning for orientation, and if the lateral interactions are not as weak as we have assumed in our analysis, then even contoured planforms can form. The second possibility stems from the observation that at low levels of V1 activity, lateral interactions are all excitatory (Hirsch & Gilbert, 1991), so that a bulk instability occurs if the homogeneous state becomes unstable, followed by secondary bifurcations to patterned planforms at the critical wavelength of $2.4 - 3.2$ mm, when the level of activity rises and the inhibition is activated. In many cases secondary bifurcations tend to be associated with complex eigenvalues, and are therefore Hopf bifurcations (Ermentrout & Cowan, 1980) that give rise to oscillations or propagating waves. In such a case it is possible for even planforms to be selected by the anistropic connectivity and odd planforms by the isotropic connectivity. In addition such a scenario is actually observed: many subjects who have taken LSD and similar hallucinogens report seeing bright white light at the center of the visual field which then explodes into a hallucinatory image (Siegel & Jarvik, 1975) in about 3 sec, corresponding to a propagation velocity in V1 of about 2.4 cm per sec. suggestive of slowly moving epileptiform activity (Milton, Mundel, an der Heiden, Spire, & Cowan, 1995; Senseman, 1999).

(c) One of the major aspects described in this paper is the presumed Euclidean symmetry of V1. Many systems exhibit Euclidean symmetry, but what is novel here is the way in which such a symmetry is generated. Thus equation (2.9) shows that the symmetry group is generated, in large part, by a translation or

shift $\{\mathbf{r}, \phi\} \to \{\mathbf{r} + \mathbf{s}, \phi\}$ followed by a rotation or twist $\{\mathbf{r}, \phi\} \to \{R_\theta \mathbf{r}, \phi + \theta\}$. It is the final twist $\phi \to \phi + \theta$ which is novel, and which is required to match the observations of G. G. Blasdel and L. Sincich [personal communication] and Bosking *et al.* (1997). In this respect it is of considerable interest that Zweck & Williams (2000) have introduced a set of basis functions with the same shift–twist symmetry as part of an algorithm to implement contour completion. Their reason for doing so is to bind sparsely distributed receptive fields together functionally, so as to perform Euclidean invariant computations. It remains to explicate the precise relationship between the Euclidean invariant circuits we have introduced here, and the Euclidean invariant receptive field models introduced by Zweck & Williams.

Figure 41: Tunnel hallucination generated by LSD. Redrawn from Oster (1970),

(d) Finally it should also be emphasized that many variants of the Klüver form constants have been described, some of which cannot be understood in terms of the simple model we have introduced. For example the Tunnel image shown in figure 41(a) exhibits a reversed retino–cortical magnification, and corresponds to images described in Knauer & Maloney (1913). It is possible that some of the circuits beyond V1, for example, those in the dorsal segment of medial superior temporal cortex (MSTd) that process radial motion, are involved in

the generation of such images, via a feedback to V1 (Morrone, Burr, & Vaina, 1995).

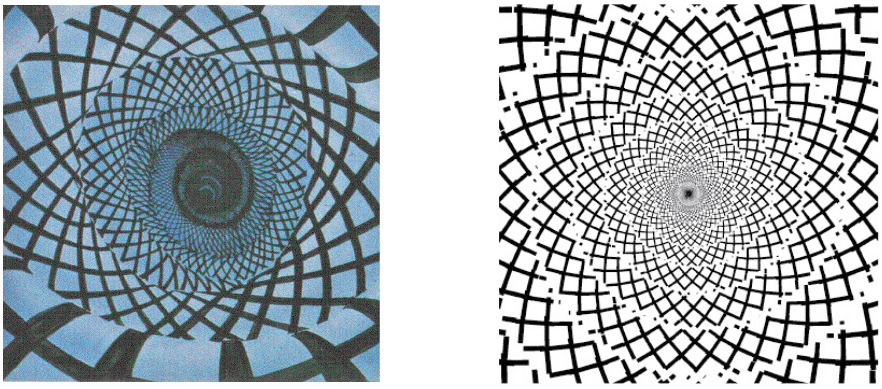

Figure 42: Left panel: Lattice–tunnel hallucination generated by Marihuana. Reproduced from Siegel (1977), with permission from Alan D. Iselin. Right panel: A simulation of the Lattice Tunnel.

Similarly, the Lattice–tunnel shown in the left panel of figure 42 is more complicated than any of the simple form constants shown earlier. One intriguing possibility is that such images are generated as a result of a mismatch between the planform corresponding to one of the Klüver form constants, and the underlying structure of V1. We have (implicitly) assumed that V1 has patchy connections that endow it with lattice properties. It should be clear from Figures 9 and 10 that such a cortical lattice is somewhat disordered. Thus one might expect some distortions to occur when planforms are spontaneously generated in such a lattice. The right panel in Figure 42 shows a computation of the appearance in the visual field of a hexagonal roll on a square lattice, when there is a slight incommensurability between the two.

As a last example we show in figure 43 another hallucinatory image triggered by LSD. Such an image does not fit very well as a form constant. However there is some secondary structure along the main (horizontal) axis of the its major components. [This is also true of the funnel and spiral images shown in figure 2,

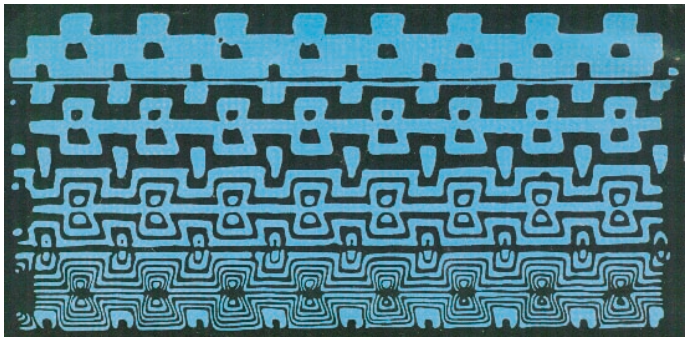

Figure 43: Complex hallucination generated by LSD. Redrawn from Oster (1970).

also triggered by LSD.] This suggests the possibility that at least two differing length scales are involved in their generation, but this is beyond the scope of the model described in the current paper. It is of interest that similar images have been reported following stimulation with flickering light (Smythies, 1960).

Acknowledgments

The authors wish to thank Drs. Alex Dimitrov, Trevor Mundel and Gary Blasdel for many helpful discussions. The authors also wish to thank the referees for a number of helpful comments, and Alan D. Eiselin for permission to reproduce his artwork in figure 42. This work was supported in part by grant 96-24 from the James S. McDonnell Foundation to JDC. The research of MG was supported in part by NSF Grant DMS-9704980. MG wishes to thank the Center for Biodynamics, Boston University for its hospitality and support. The research of PCB was supported by a grant from the Leverhulme Trust. PCB wishes to thank the Mathematics Department, University of Chicago for its hospitality and support. PCB and JDC also wish to thank Prof. Geoffrey Hinton FRS and the Gatsby Computational Neurosciences Unit, University College, London for hospitality and support. PJT was supported, in part, by NIH grant T-32-MH20029 and by the Alfred P. Sloan Foundation.

A Appendices

A.1 Perturbation expansion of the eigenfunctions

We summarize here the derivation of equations (3.13)–(3.15). This involves solving the matrix equation

$$\left[\frac{\lambda+\alpha}{\sigma_1\mu} - W_m\right] A_m = \beta \sum_{n\in\mathbf{Z}} \hat{W}_{m-n}(q) A_n \tag{A.1}$$

using a standard application of degenerate perturbation theory. That is, we introduce the perturbation expansions

$$\frac{\lambda+\alpha}{\sigma_1\mu} = W_1 + \beta\lambda^{(1)} + \beta^2\lambda^{(2)} + \dots \tag{A.2}$$

$$A_n = z_{\pm 1}\delta_{n,\pm 1} + \beta A_n^{(1)} + \beta^2 A_n^{(2)} + \dots \tag{A.3}$$

and substitute these into the eigenvalue equation (3.10). We then systematically solve the resulting hierarchy of equations to successive orders in β.

$\mathcal{O}(\beta)$ terms Setting $m = 1$ in equation (A.1) yields the $\mathbf{O}(\beta)$ equation

$$\hat{W}_0(q)z_1 + \hat{W}_2(q)z_{-1} = \lambda^{(1)} z_1$$

Combining this with the conjugate equation $m = -1$ we obtain the matrix equation

$$\begin{pmatrix} \hat{W}_0(q) & \hat{W}_2(q) \\ \hat{W}_{-2}(q) & \hat{W}_0(q) \end{pmatrix} \begin{pmatrix} z_1 \\ z_{-1} \end{pmatrix} = \lambda^{(1)} \begin{pmatrix} z_1 \\ z_{-1} \end{pmatrix} \tag{A.4}$$

Equation (A.4) has solutions of the form

$$\lambda^{(1)} = \hat{W}_0(q) \pm \hat{W}_2(q) \tag{A.5}$$

$$z_{-1} = \pm z_1 \tag{A.6}$$

where + and − denote the even and odd solutions. We have used the result $\hat{W}_{-2} = \hat{W}_2$. The $\mathcal{O}(\beta)$ terms in equation (A.1) for which $m \neq \pm 1$ generate the corresponding first-order amplitudes

$$A_m^{(1)} = \frac{\hat{W}_{m-1}(q)z_1 + \hat{W}_{m+1}(q)z_{-1}}{W_1 - W_m} \tag{A.7}$$

$\mathcal{O}(\beta^2)$ terms The $\mathcal{O}(\beta^2)$ contribution to equation (A.1) for $m = 1$ is

$$\sum_{n\neq\pm 1} \hat{W}_{1-n}(q)A_n^{(1)} + \left[\hat{W}_0(q) - \lambda^{(1)}\right] A_1^{(1)} + \hat{W}_2(q)A_{-1}^{(1)} = \lambda^{(2)} z_1$$

Combining with the analogous equation for $m = -1$ yields the matrix equation

$$\begin{pmatrix} \hat{W}_0(q) - \lambda^{(1)} & \hat{W}_2(q) \\ \hat{W}_{-2}(q) & \hat{W}_0(q) - \lambda^{(1)} \end{pmatrix} \begin{pmatrix} A_1^{(1)} \\ A_{-1}^{(1)} \end{pmatrix} = \begin{pmatrix} B_1(q) \\ B_{-1}(q) \end{pmatrix} \tag{A.8}$$

where

$$B_1(q) = \lambda^{(2)} z_1 - \sum_{n\neq\pm 1} \hat{W}_{1-n}(q)A_n^{(1)} \tag{A.9}$$

Multiplying both sides of equation (A.8) on the left by (z_{-1}, z_1) and using equation (A.4) implies that $B_1(q) = 0$. This together with equation (A.7) determines the second–order contribution to the eigenvalue:

$$\lambda^{(2)} = \sum_{m\neq 1, m\geq 0} \frac{\left[\hat{W}_{1-m}(q) \pm \hat{W}_{1+m}(q)\right]^2}{W_1 - W_m} \tag{A.10}$$

Having obtained $\lambda^{(2)}$ we can then use equations (A.8) and (A.5) to obtain the result

$$A_{-1}^{(1)} = \pm A_1^{(1)} \tag{A.11}$$

The unknown amplitudes z_1 and $A_1^{(1)}$ are determined by the overall normalization of the solution.

Finally, combining equations (A.2), (A.5), (A.6), and (A.10) generates equation (3.13). Similarly, combining equations (A.3), (A.6), (A.7), (A.11) and (3.7) yields the pair of equations (3.14) and (3.15).

A.2 Construction of axial subgroups

We sketch how to construct the axial subgroups from the irreducible representations of the holohedry $H_{\mathcal{L}}$ corresponding to the shortest dual wave vectors as given in Table 2. By rescalings we can assume that the critical wavenumber $q_c = 1$ and that the doubly periodic functions are on a lattice $\mathcal{L}$ whose dual lattice $\mathcal{L}^*$ is generated by wave vectors of length

1. There are two types of irreducible representations for each lattice corresponding to the cases $u(\phi)$ odd and $u(\phi)$ even. We derive the explicit action of $\Gamma_{\mathcal{L}}$ on these subspaces and determine the axial subgroups.

The action of the torus $\mathbf{T}^2$ on the subspace $K_{\mathcal{L}}$ is derived as follows. Write $\theta \in \mathbf{T}^2$ as

$$\theta = 2\pi\theta_1\boldsymbol{\ell}_1 + 2\pi\theta_2\boldsymbol{\ell}_2.$$

Using the fact that $\mathbf{k}_i \cdot \boldsymbol{\ell}_j = \delta_{ij}$, the result of the translation action is given in Table 5.

Lattice	Torus Action
Square	$(e^{2\pi i\theta_1}c_1, e^{2\pi i\theta_2}c_2)$
Hexagonal	$(e^{2\pi i\theta_1}c_1, e^{2\pi i\theta_1}c_2, e^{-2\pi i(\theta_1+\theta_2)}c_3)$
Rhombic	$(e^{2\pi i\theta_1}c_1, e^{2\pi i\theta_2}c_2)$

Table 5: Torus action on $\Gamma_{\mathcal{L}}$-irreducible representation.

The holohedries $H_{\mathcal{L}}$ are $\mathbf{D}_4$, $\mathbf{D}_6$, and $\mathbf{D}_2$ for the square, hexagonal, and rhombic lattices, respectively. In each case the generators for these groups are a reflection and a rotation. For the square and hexagonal lattices, the reflection is κ, the reflection across the x axis where $\mathbf{r} = (x, y)$. For the rhombic lattice, the reflection is κ_η. The counterclockwise rotation ξ, through angles $\frac{\pi}{2}$, $\frac{\pi}{3}$, and π, is the rotation generator for the three lattices. The action of $H_{\mathcal{L}}$ for the various lattices is given in Table 6.

Finally, for each of the six types of irreducible representations, we compute the axial subgroups, those isotropy subgroups Σ that have one–dimensional fixed–point subspaces $\mathrm{Fix}(\Sigma)$, in each irreducible representation. The computations for the square and rhombic lattices are straightforward since we can use the $\mathbf{T}^2$-action in Table 5 to assume, after conjugacy, that c_1 and c_2 are real and nonnegative. The computations on the hexagonal lattice are more complicated (Bressloff *et al.*, 2000b). The results, up to conjugacy, are listed in Tables 7 and 8.

$\mathbf{D}_2$	Action	$\mathbf{D}_4$	Action	$\mathbf{D}_6$	Action
$\mathbf{1}$	(c_1, c_2)	$\mathbf{1}$	(c_1, c_2)	$\mathbf{1}$	(c_1, c_2, c_3)
ξ	$(\overline{c_1}, \overline{c_2})$	ξ	$(\overline{c_2}, c_1)$	ξ	$(\overline{c_2}, \overline{c_3}, \overline{c_1})$
κ_η	$\epsilon(c_2, c_1)$	ξ^2	$(\overline{c_1}, \overline{c_2})$	ξ^2	(c_3, c_1, c_2)
$\kappa_\eta\xi$	$\epsilon(\overline{c_2}, \overline{c_1})$	ξ^3	$(c_2, \overline{c_1})$	ξ^3	$(\overline{c_1}, \overline{c_2}, \overline{c_3})$
		κ	$\epsilon(c_1, \overline{c_2})$	ξ^4	(c_2, c_3, c_1)
		$\kappa\xi$	$\epsilon(\overline{c_2}, \overline{c_1})$	ξ^5	$(\overline{c_3}, \overline{c_1}, \overline{c_2})$
		$\kappa\xi^2$	$\epsilon(\overline{c_1}, c_2)$	κ	$\epsilon(c_1, c_3, c_2)$
		$\kappa\xi^3$	$\epsilon(c_2, c_1)$	$\kappa\xi$	$\epsilon(\overline{c_2}, \overline{c_1}, \overline{c_3})$
				$\kappa\xi^2$	$\epsilon(c_3, c_2, c_1)$
				$\kappa\xi^3$	$\epsilon(\overline{c_1}, \overline{c_3}, \overline{c_2})$
				$\kappa\xi^4$	$\epsilon(c_2, c_1, c_3)$
				$\kappa\xi^5$	$\epsilon(\overline{c_3}, \overline{c_2}, \overline{c_1})$
$[\theta_1, \theta_2]$	$(e^{-2\pi i\theta_1}c_1, e^{-2\pi i\theta_2}c_2)$			$(e^{-2\pi i\theta_1}c_1, e^{-2\pi i\theta_2}c_2, e^{2\pi i(\theta_1+\theta_2)}c_3)$	

Table 6: (Left) $\mathbf{D}_2\dot{+}\mathbf{T}^2$ action on rhombic lattice; (Center) $\mathbf{D}_4\dot{+}\mathbf{T}^2$ action on square lattice; (Right) $\mathbf{D}_6\dot{+}\mathbf{T}^2$ action on hexagonal lattice. For $u(\phi)$ even, $\epsilon = +1$; for $u(\phi)$ odd, $\epsilon = -1$.

Lattice	Subgroup Σ	Fix(Σ)	Name
square	$\mathbf{D}_4(\kappa, \xi)$	(1,1)	even square
	$\mathbf{O}(2) \oplus \mathbf{Z}_2(\kappa)$	(1,0)	even roll
rhombic	$\mathbf{D}_2(\kappa_\eta, \xi)$	(1,1)	even roll
	$\mathbf{O}(2)$	(1,0)	even rhombic
hexagonal	$\mathbf{D}_6(\kappa, \xi)$	(1,1,1)	even hexagon (0)
	$\mathbf{D}_6(\kappa, \xi)$	(-1,-1,-1)	even hexagon (π)
	$\mathbf{O}(2) \oplus \mathbf{Z}_2(\kappa)$	(1,0,0)	even roll

Table 7: Axial subgroups when $u(-\phi) = u(\phi)$. $\mathbf{O}(2)$ is generated by $[0, \theta_2] \in \mathbf{T}^2$ and rotation by π (ξ on rhombic lattice, ξ^2 on square lattice, and ξ^3 on hexagonal lattice). The points $(1, 1, 1)$ and $(-1, -1, -1)$ have the same isotropy subgroup ($\mathbf{D}_6$) — but are not conjugate by a group element. Therefore, the associated eigenfunctions generate different planforms.

Lattice	Subgroup Σ	Fix(Σ)	Name
square	$\mathbf{D}_4\left(\kappa\left[\frac{1}{2},\frac{1}{2}\right],\xi\right)$	(1,-1)	odd square
	$\mathbf{O}(2)\oplus\mathbf{Z}_2\left(\xi^2\kappa\left[\frac{1}{2},0\right]\right)$	(1,0)	odd roll
rhombic	$\mathbf{D}_2\left(\kappa_\eta\left[\frac{1}{2},\frac{1}{2}\right],\xi\right)$	(1,1)	odd rhombic
	$\mathbf{O}(2)\oplus\mathbf{Z}_2\left(\xi^2\kappa\left[\frac{1}{2},0\right]\right)$	(1,0)	odd roll
hexagonal	$\mathbf{Z}_6(\xi)$	(1,1,1)	odd hexagon
	$\mathbf{D}_3(\kappa\xi,\xi^2)$	(i,i,i)	triangle
	$\mathbf{D}_2(\kappa,\xi^3)$	(0,1,-1)	patchwork quilt
	$\mathbf{O}(2)\oplus\mathbf{Z}_4\left(\xi^3\kappa\left[\frac{1}{2},0\right]\right)$	(1,0,0)	odd roll

Table 8: Axial subgroups when $u(-\phi)=-u(\phi)$. $\mathbf{O}(2)$ is generated by $[0,\theta_2]\in\mathbf{T}^2$ and rotation by π (ξ on rhombic lattice, ξ^2 on square lattice, and ξ^3 on hexagonal lattice).

A.3 Derivation of the amplitude equation

Assume that sufficiently close to the bifurcation point at which the homogeneous state $a(\mathbf{r},\phi)=0$ becomes marginally stable, the excited modes grow slowly at a rate $\mathcal{O}(\epsilon^2)$ where $\epsilon^2=\mu-\mu_c$. We use the method of multiple–scales to derive the cubic amplitude equations (6.2) and (6.5).

Multiple–scale analysis We begin by rewriting equation (2.11) in the more compact form

$$\frac{da}{dt}=-\alpha a+\mu w*\sigma[a] \tag{A.12}$$

with

$$w*\sigma[a]=\int_0^\pi w_{loc}(\phi-\phi')\sigma[a(\mathbf{r},\phi',t)]d\phi'+\beta\int_{\mathbf{R}^2}w_{lat}(\mathbf{r}-\mathbf{r}',\phi)\sigma[a(\mathbf{r}',\phi,t)]d\mathbf{r}' \tag{A.13}$$

$\mu=\mu_c+\epsilon^2$. Taylor expand the nonlinear function $\sigma[a]$ appearing in equation (A.12):

$$\sigma[a]=\sigma_1 a+\sigma_2 a^2+\sigma_3 a^3+\dots$$

where $\sigma_1=\sigma'[0]$, $\sigma_2=\sigma''[0]/2$, $\sigma_3=\sigma'''[0]/3!$ etc. Then perform a perturbation expansion of equation (A.12) with respect to ϵ by writing

$$a=\epsilon a_1+\epsilon^2 a_2+\dots$$

and introducing a slow time-scale $\tau = \epsilon^2 t$. Collecting terms with equal powers of ϵ then generates a hierarchy of equations of the form

$$\mathsf{L}a_1 = 0, \quad \mathsf{L}a_n = b_n, n > 1 \tag{A.14}$$

where

$$\mathsf{L}a = \alpha a - \mu_c \sigma_1 w * a$$

and

$$b_2 = \mu_c \sigma_2 w * a_1^2 \tag{A.15}$$

$$b_3 = \mu_c \sigma_3 w * a_1^3 + 2\mu_c \sigma_2 w * a_1 a_2 - \left[\frac{da_1}{d\tau} - \sigma_1 w * a_1 \right] \tag{A.16}$$

Solvability conditions The first equation in the hierarchy is equivalent to the eigenvalue equation (3.10) with $\lambda = 0$, $\mu = \mu_c$ and $|\mathbf{k}| = q_c$. Therefore, the relevant classes of solution are of the form (6.1):

$$a_1(\mathbf{r}, \phi, t) = \sum_{j=1}^{N} c_j(t) \mathrm{e}^{i\mathbf{k}_j \cdot \mathbf{r}} u(\phi - \varphi_j) + c.c. \tag{A.17}$$

Following §4 we restrict solutions to the space of doubly periodic functions on a square or rhombic lattice ($N = 2$) or a hexagonal lattice ($N = 3$). Next define the inner product of two arbitrary functions $a(\mathbf{r}, \phi)$, $b(\mathbf{r}, \phi)$ according to

$$\langle a|b\rangle = \int_\Omega \int_0^\pi \overline{a}(\mathbf{r}, \phi) b(\mathbf{r}, \phi) \frac{d\phi}{\pi} d\mathbf{r}$$

where Ω is a fundamental domain of the periodically tiled plane (whose area is normalized to unity). The linear operator L is self-adjoint with respect to this inner product, that is, $\langle a|\mathsf{L}b\rangle = \langle \mathsf{L}a|b\rangle$. Therefore, defining

$$v_l(\mathbf{r}, \phi) = \mathrm{e}^{i\mathbf{k}_l \cdot \mathbf{r}} u(\phi - \varphi_l),$$

we have $\langle v_l|\mathsf{L}a_n\rangle = \langle \mathsf{L}v_l|a_n\rangle = 0$ for $n = 2, 3, \ldots$. Since $\mathsf{L}a_n = b_n$, we obtain a hierarchy of solvability conditions

$$\langle v_l|b_n\rangle = 0$$

From equation (A.15) the lowest order solvability condition is $\mu_c\sigma_2\langle v_l|w*a_1^2\rangle=0$. It turns out that in the presence of lateral interactions the inner product $\langle v_l|w*a_1^2\rangle$ can be non-vanishing (in the case of even patterns) which leads to a contradiction when $\sigma_2\neq 0$. This can be remedied by assuming that $\sigma_2=\epsilon\sigma_2'+\mathcal{O}(\epsilon^2)$ and considering the modified solvability condition $\langle v_l|\epsilon^{-1}b_2+b_3\rangle=0$. This generates the equation

$$\langle v_l|\frac{da_1}{d\tau}-\sigma_1 w*a_1\rangle=\mu_c\sigma_3\langle v_l|w*a_1^3\rangle+\mu_c\sigma_2'\langle v_l|w*a_1^2\rangle \tag{A.18}$$

An alternative approach to handling the non-vanishing of the inner product $\langle v_l|w*a_1^2\rangle$ would be to expand the bifurcation parameter as $\mu=\mu_c+\epsilon\mu_1+\epsilon^2\mu_2+\ldots$. This would then give a quadratic (rather than a cubic) amplitude equation describing the growth of unstable hexagonal patterns. In the case of odd patterns $\langle v_l|w*a_1^2\rangle\equiv 0$ and no restriction on σ_2 is required. However, for ease of exposition we treat the odd and even cases in the same way.

Amplitude equations In order to explicitly derive the amplitude equations (6.2) and (6.5) from the solvability condition (A.18), we need to evaluate inner products of the form $\langle v_l|w*a_1^n\rangle$. Since v_l is a solution to the linear equation (A.14), it follows that

$$\langle v_l|w*a_1^n\rangle=\langle w*v_l|a_1^n\rangle=\frac{\alpha}{\mu_c\sigma_1}\langle v_l|a_1^n\rangle \tag{A.19}$$

Thus, substituting equation (A.17) into the left-hand side of equation (A.18) and using (A.19) shows that

$$\langle v_l|\frac{da_1}{d\tau}-\sigma_1 w*a_1\rangle=\left[1+\Gamma^{(1)}\right]\frac{dc_l}{d\tau}-\left[\sigma_1 W_{01}+\hat{\Gamma}^{(1)}\right]c_l \tag{A.20}$$

with $\Gamma^{(1)},\hat{\Gamma}^{(1)}=\mathcal{O}(\beta)$. The β–dependent factors appearing on the right–hand side of equation (A.20) are eliminated from the final amplitude equations by an appropriate rescaling of the time τ and a global rescaling of the amplitudes c_j. Similarly,

$$\langle v_l|a_1^2\rangle=\Gamma^{(2)}\sum_{i,j=1}^{3}\overline{c}_i\overline{c}_j\delta(\mathbf{k}_i+\mathbf{k}_j+\mathbf{k}_l) \tag{A.21}$$

and

$$\langle v_l|a_1^3\rangle=3c_l\left[\Gamma^{(3)}(0)|c_l|^2+2\sum_{j\neq l}\Gamma^{(3)}(\varphi_j-\varphi_l)|c_j|^2\right] \tag{A.22}$$

with $\Gamma^{(2)}$ and $\Gamma^{(3)}$ given by equations (6.12) and (6.13). Note from equation (A.21) that the inner product $\langle v_l | a_1^2 \rangle$ is only nonvanishing when $N = 3$ (corresponding to hexagonal planforms) since we require $\sum_{j=1}^{N} \mathbf{k}_j = 0$. One possible set of wave vectors is $\mathbf{k}_j = q_c(\cos(\varphi_j), \sin(\varphi_j))$ with $\varphi_1 = 0, \varphi_2 = 2\pi/3, \varphi_3 = -2\pi/3$. Also note that if $u(\phi)$ is an odd eigenfunction then it immediately follows that $\Gamma^{(2)} = 0$.

Finally, substitute equations (A.19), (A.20), (A.21) and (A.22) into (A.18) and perform the rescaling $\epsilon c_l \to \sqrt{\sigma_1 W_1 + \hat{\Gamma}^{(1)}} c_l$. After an additional rescaling of time we obtain the amplitude equation (6.2) for $N = 2$ and (6.5) for $N = 3$.

References

Blasdel, G. G., 1992. Orientation selectivity, preference, and continuity in monkey striate cortex. *J. Neurosci.* **12**: 3139–3161.

Bosch Vivancos, I., Chossat, P., & Melbourne, I., 1995. New planforms in systems of partial differential equations with euclidean symmetry. *Arch. Rat. Mech.* **131**: 199–224.

Bosking, W. H., Zhang, Y., Schofield, B., & Fitzpatrick, D., 1997. Orientation selectivity and the arrangement of horizontal connections in tree shrew striate cortex. *J. Neurosci.* **17**: 2112–2127.

Bressloff, P. C., Bressloff, N. W., & Cowan, J. D., 2000a. Dynamical mechanism for sharp orientation tuning in an integrate-and-fire model of a cortical hypercolumn. *Neural Comput.* **12** (11): 2473–2512.

Bressloff, P. C., Cowan, J. D., Golubitsky, M., & Thomas, P. J., 2000b. Scalar and pseudoscalar bifurcations: pattern formation in the visual cortex. Submitted for publication.

Busse, F. H., 1962. Das stabilitätsverhalten der zellular konvektion bei endlicher amplitude. *Ph.D Dissertation, University of Munich.* Engl. trans. by S. H. Davis, Rand Report LT-66-19.

Buzano, E. & Golubitsky, M., 1983. Bifurcation involving the hexagonal lattice and the planar bénard problem. *Phil. Trans. Roy. Soc. London* **A 308**: 617–667.

Clottes, J. & Lewis-Williams, D., 1998. *The Shamans of Prehistory: Trance and Magic in the Painted Caves*. New York: Abrams.

Cowan, J. D., 1977. Some remarks on channel bandwidths for visual contrast detection. *Neurosciences Research Program Bull.* **15**: 492–517.

Cowan, J. D., 1982. Spontaneous symmetry breaking in large scale nervous activity. *Intl. J. Quantum Chem.* **22**: 1059–1082.

Cowan, J. D., 1997. Neurodynamics and brain mechanisms. In *Cognition, Computation, and Consciousness*, (eds. M. Ito, Y. Miyashita, & E. T. Rolls), pp. 205–233. Oxford University Press.

Drasdo, N., 1977. The neural representation of visual space. *Nature* **266**: 554–556.

Dybowski, M., 1939. Conditions for the appearance of hypnagogic visions. *Kwart. Psychol.* **11**: 68–94.

Ermentrout, G. B., 1991. Spots or stripes. *Proc. Roy. Soc. A* **434**: 413–428.

Ermentrout, G. B., 1998. Neural networks as spatial pattern forming systems. *Rep. Prog. Phys.* **61**: 353–430.

Ermentrout, G. B. & Cowan, J. D., 1979. A mathematical theory of visual hallucination patterns. *Biol. Cybernetics* **34**: 137–150.

Ermentrout, G. B. & Cowan, J. D., 1980. Secondary bifurcation in neuronal nets. *SIAM J. Applied Math.* **39**: 323–340.

Eysel, U., 1999. Turning a corner in vision research. *Nature* **399**: 641–644.

Gilbert, C. D., 1992. Horizontal integration and cortical dynamics. *Neuron* **9**: 1–13.

Gilbert, C. D. & Wiesel, T. N., 1983. Clustered intrinsic connections in cat visual cortex. *J. Neurosci.* **3**: 1116–1133.

Golubitsky, M., Stewart, I., & Schaeffer, D. G., 1988. *Singularities and Groups in Bifurcation Theory II*. Berlin: Springer-Verlag.

Golubitsky, M., Swift, J. W., & Knobloch, E., 1984. Symmetries and pattern selection in rayleigh–bénard convection. *Physica D* **10**: 249–276.

Hansel, D. & Sompolinsky, H., 1997. Modeling feature selectivity in local cortical circuits. In *Methods of Neuronal Modeling*, (eds. C. Koch & I. Segev), pp. 499–567. Cambridge: MIT Press, 2nd edition.

Helmholtz, H., 1925. *Physiological Optics*, volume II. Rochester, N.Y.: Optical Soc. Amer.

Hirsch, J. D. & Gilbert, C. D., 1991. Synaptic physiology of horizontal connections in the cat's visual cortex. *J. Neurosci.* **11**: 1800–1809.

Horton, J. C., 1996. Pattern of ocular dominance columns in human striate cortex in strabismic amblyopia. *Visual Neurosci.* **13**: 787–795.

Hubel, D. H. & Wiesel, T. N., 1967. Cortical and callosal connections concerned with the vertical meridian in the cat. *J. Neurophysiol.* **30**: 1561–1573.

Hubel, D. H. & Wiesel, T. N., 1974a. Sequence regularity and geometry of orientation columns in the monkey striate cortex. *J. Comp. Neurol.* **158**: 267–294.

Hubel, D. H. & Wiesel, T. N., 1974b. Uniformity of monkey striate cortex: A parallel relationship between field size, scatter, and magnification factor. *J. Comp. Neurol.* **158**: 295–306.

Ishai, A. & Sagi, D., 1995. Common mechanisms of visual imagery and perception. *Science* **268**: 1772–1774.

Klüver, H., 1966a. *Mescal and Mechanisms of Hallucinations*. University of Chicago Press.

Klüver, H., 1966b. *Mescal and Mechanisms of Hallucinations*. University of Chicago Press.

Knauer, A. & Maloney, W. J., 1913. A preliminary note on the psychic action of mescalin, with special reference to the mechanism of visual hallucinations. *J. Nerv. Ment. Dis.* **40**: 425–436.

Kosslyn, S. M., 1994. *Image and Brain*. Cambridge: MIT Press.

Krill, A. E., Alpert, H. J., & Ostfield, A. M., 1963. Effects of a hallucinogenic agent in totally blind subjects. *Arch. Opthalmol.* **69**: 180–185.

Lee, T. S., Mumford, D., Romero, R., & Lamme, V. A. F., 1998. The role of primary visual cortex in higher level vision. *Vision Research* **38**: 2429–2454.

Levitt, J. B. & Lund, J., 1997. Contrast dependence of contextual effects in primate visual cortex. *Nature* **387**: 73–76.

Li, Z., 1999. Pre-attentive segmentation in the primary visual cortex. *Spatial Vision* **13**: 25–50.

Livingstone, M. S. & Hubel, D. H., 1984. Specificity of intrinsic connections in primate primary visual cortex. *J. Neurosci.* **4**: 2830–2835.

McGuire, B. A., Gilbert, C. D., Rivlin, P. K., & Wiesel, T. N., 1991. Targets of horizontal connections in macaque primary visual cortex. *J. Comp. Neurol.* **305**: 370–392.

Milton, J., Mundel, T., an der Heiden, U., Spire, J.-P., & Cowan, J. D., 1995. Traveling activity waves. In *The Handbook of Brain Theory and Neural Networks*, (ed. M. A. Arbib), pp. 994–997. Cambridge: MIT Press.

Mitchison, G. & Crick, F., 1982. Long axons within the striate cortex: their distribution, orientation, and patterns of connection. *Proc. Nat. Acad. Sci. (USA)* **79**: 3661–3665.

Miyashita, Y., 1995. How the brain creates imagery: Projection to primary visual cortex. *Science* **268**: 1719–1720.

Morrone, M. C., Burr, D. C., & Vaina, L. M., 1995. Two stages of visual processing for radial and circular motion. *Nature* **376**: 507–509.

Mourgue, R., 1932. *Neurobiologie de l'hallucination*. Lamertin: Brussels.

Mundel, T., Dimitrov, A., & Cowan, J. D., 1997. Visual cortex circuitry and orientation tuning. In *Advances in Neural Information Processing Systems*, (eds. M. C. Mozer, M. I. Jordan, & T. Petsche), volume 9, pp. 887–893. Cambridge: MIT Press.

Oster, G., 1970. Phosphenes. *Scientific American* **222** (2): 83–87.

Patterson, A., 1992. *Rock Art Symbols of the Greater Southwest*. Boulder CO: Johnson Books.

Purkinje, J. E., 1918. *Opera omnia*, volume 1. Prague: Society of Czech Physicians.

Rockland, K. S. & Lund, J., 1983. Intrinsic laminar lattice connections in primate visual cortex. *J. Comp. Neurol.* **216**: 303–318.

Schwartz, E., 1977. Spatial mapping in the primate sensory projection: analytic structure and relevance to projection. *Biol. Cybernetics* **25**: 181–194.

Senseman, D. M., 1999. Spatiotemporal structure of depolarization spread in cortical pyramidal cell populations evoked by diffuse retinal light flashes. *Visual Neuroscience* **16**: 65–79.

Sereno, M. I., Dale, A. M., Reppas, J. B., Kwong, K. K., Belliveau, J. W., Brady, T. J., Rosen, B. R., & Tootell, R. B. H., 1995. Borders of multiple visual areas in humans revealed by functional magnetic resonance imaging. *Science* **268**: 889–893.

Siegel, R. K., 1977. Hallucinations. *Scientific American* **237** (4): 132–140.

Siegel, R. K. & Jarvik, M. E., 1975. Drug-induced hallucinations in animals and man. In *Hallucinations: Behavior, Experience and Theory*, (eds. R. K. Siegel & L. J. West), pp. 81–161. New York: Wiley.

Smythies, J. R., 1960. The stroboscopic patterns iii. further experiments and discussion. *Brit. J. Psychol.* **51** (3): 247–255.

Turing, A. M., 1952. The chemical basis of morphogenesis. *Phil. Trans. Roy Soc. Lond. B* **237**: 32–72.

Tyler, C. W., 1978. Some new entoptic phenomena. *Vision Res.* **181**: 1633–1639.

Tyler, C. W., 1982. Do grating stimuli interact with the hypercolumn spacing in the cortex? *Suppl. Invest. Opthalmol.* **222**: 254.

von der Malsburg, C. & Cowan, J. D., 1982. Outline of a theory for the ontogenesis of iso-orientation domains in visual cortex. *Biol. Cybern.* **45**: 49–56.

Walgraef, D., 1997. *Spatio-temporal pattern formation*. New York: Springer-Verlag.

Wiener, M. C., 1994. *Hallucinations, Symmetry, and the Structure of Primary Visual Cortex: a Bifurcation Theory Approach*. Ph.D. thesis, University of Chicago, Chicago, Illinois, USA.

Wilson, H. R. & Cowan, J. D., 1972. Excitatory and inhibitory interactions in localized populations of model neurons. *Biophysical J.* **12**: 1–24.

Wilson, H. R. & Cowan, J. D., 1973. A mathematical theory of the functional dynamics of cortical and thalamic nervous tissue. *Kybernetik* **13**: 55–80.

Winters, W. D., 1975. The continuum of CNS excitatory states and hallucinosis. In *Hallucinations: Behavior, Experience and Theory*, (eds. R. K. Siegel & L. J. West), pp. 53–70. New York: Wiley.

Zweck, J. W. & Williams, L. R., 2000. Euclidean group invariant computation of stochastic completion fields using shiftable-twistable functions. Submitted for publication.